

HOT X-RAY CORONAE AROUND MASSIVE SPIRAL GALAXIES: A UNIQUE PROBE OF STRUCTURE FORMATION MODELS

ÁKOS BOGDÁN^{1,4}, WILLIAM R. FORMAN¹, MARK VOGELSBERGER¹,
HERVÉ BOURDIN², DEBORA SIJACKI¹, PASQUALE MAZZOTTA^{1,2}, RALPH P. KRAFT¹,
CHRISTINE JONES¹, MARAT GILFANOV³, EUGENE CHURAZOV³, AND LAURENCE P. DAVID¹

¹Harvard Smithsonian Center for Astrophysics, 60 Garden Street, Cambridge, MA 02138, USA; abogdan@cfa.harvard.edu

²Dipartimento di Fisica, Università degli Studi di Roma “Tor Vergata”, via della Ricerca Scientifica 1, 00133 Roma, Italy and

³Max-Planck-Institut für Astrophysik, Karl-Schwarzschild-str. 1, 85748 Garching, Germany

Draft version October 31, 2018

ABSTRACT

Luminous X-ray gas coronae in the dark matter halos of massive spiral galaxies are a fundamental prediction of structure formation models, yet only a few such coronae have been detected so far. In this paper, we study the hot X-ray coronae beyond the optical disks of two “normal” massive spirals, NGC1961 and NGC6753. Based on *XMM-Newton* X-ray observations, hot gaseous emission is detected to ~ 60 kpc – well beyond their optical radii. The hot gas has a best-fit temperature of $kT \sim 0.6$ keV and an abundance of ~ 0.1 Solar, and exhibits a fairly uniform distribution, suggesting that the quasi-static gas resides in hydrostatic equilibrium in the potential well of the galaxies. The bolometric luminosity of the gas in the $(0.05 - 0.15)r_{200}$ region (r_{200} is the virial radius) is $\sim 6 \times 10^{40}$ erg s⁻¹ for both galaxies. The baryon mass fractions of NGC1961 and NGC6753 are $f_{b,NGC1961} \sim 0.11$ and $f_{b,NGC6753} \sim 0.09$, which values fall short of the cosmic baryon fraction. The hot coronae around NGC1961 and NGC6753 offer an excellent basis to probe structure formation simulations. To this end, the observations are confronted with the moving mesh code AREPO and the smoothed particle hydrodynamics code GADGET. Although neither model gives a perfect description, the observed luminosities, gas masses, and abundances favor the AREPO code. Moreover, the shape and the normalization of the observed density profiles are better reproduced by AREPO within $\sim 0.5r_{200}$. However, neither model incorporates efficient feedback from supermassive black holes or supernovae, which could alter the simulated properties of the X-ray coronae. With the further advance of numerical models, the present observations will be essential in constraining the feedback effects in structure formation simulations.

Subject headings: galaxies: individual (NGC1961, NGC6753) — galaxies: spiral — galaxies: ISM — X-rays: galaxies — X-rays: general — X-rays: ISM

1. INTRODUCTION

The presence of hot gaseous coronae in dark matter halos of massive galaxies is a fundamental prediction of structure formation models (White & Rees 1978). This gas collapse scenario in a cold dark matter dominated Universe was applied by White & Rees (1991), who predicted that dark matter halos – surrounding all types of present epoch massive galaxies – should have an associated X-ray luminous corona.

X-ray luminous, hot gaseous coronae are nearly ubiquitous for massive early-type galaxies. First discovered with the *Einstein Observatory* (Forman et al. 1985), these coronae have been extensively studied (e.g. Sarazin et al. 2001; Jones et al. 2002; Mathews & Brighenti 2003; Bogdán & Gilfanov 2011b). Early-type galaxies exhibit at least three X-ray emitting components. (1) A well-studied population of low-mass X-ray binaries (LMXBs), which add a notable contribution to the total X-ray emission of galaxies (Gilfanov 2004; Zhang et al. 2012); (2) emission from active binaries (ABs) and cataclysmic variables (CVs), whose total emission is proportional to the stellar mass of the galaxy (e.g. Revnivtsev et al. 2008; Bogdán & Gilfanov 2011b), and (3) thermal, sub-keV gas, produced from

the galaxy's own constituent stars or from infall of group/cluster gas in central bright cluster galaxies. For massive early-type galaxies, it is difficult to detect the more extended atmospheres of hot gas, since they either have bright coronae from stellar mass loss and/or lie in larger dark matter halos - groups and clusters - that have their own gaseous atmospheres. Thus, elliptical galaxies are not suitable for probing the luminous X-ray gas predicted around individual galaxies.

However, late-type, spiral galaxies, also are predicted to have luminous X-ray coronae and can test galaxy formation scenarios (White & Rees 1991). A major advantage of spirals is their location: whereas massive ellipticals lie either in the center of galaxy groups and clusters and/or in rich environments, it is possible to find relatively isolated and quiescent massive spiral galaxies. Starburst galaxies or galaxies undergoing mergers are not suitable to characterize the extraplanar X-ray emission. Thanks to UV, far-infrared, and H α imaging, large star-formation rates, hence starburst galaxies, can be identified, and merging galaxies can be recognized based on their optical appearance. Thus, isolated massive spiral galaxies with moderately low star formation rates and relatively undisturbed morphology are the ideal targets for exploring the extraplanar X-ray coronae, thereby testing structure formation models.

⁴Einstein Fellow

TABLE 1
THE PROPERTIES OF THE SAMPLE GALAXIES.

Name	Distance	1' scale	N_H	L_K	M_*/L_K	M_*	SFR	Morph.	r_{200}	T_{obs}
	(Mpc)	(kpc)	(cm^{-2})	($L_{K,\odot}$)	($M_\odot/L_{K,\odot}$)	(M_\odot)	($M_\odot \text{ yr}^{-1}$)	type	(kpc)	(ks)
	(1)	(2)	(3)	(4)	(5)	(6)	(7)	(8)	(9)	(10)
NGC1961	55.8	16.23	8.4×10^{20}	5.4×10^{11}	0.78	4.2×10^{11}	15.5	SAB(rs)c	470	73.7
NGC6753	43.6	12.67	5.5×10^{20}	3.9×10^{11}	0.81	3.2×10^{11}	11.8	(R)SA(r)b	440	73.9

Note. Columns are as follows. (1) Distance taken from NED (<http://nedwww.ipac.caltech.edu/>). (2) 1' scale at the applied distance. (3) Galactic absorption (Dickey & Lockman 1990). (4) Total K-band luminosity. (5) K-band mass-to-light ratios computed from Bell et al. (2003) using the $B - V$ color indices of galaxies (de Vaucouleurs et al. 1991). (6) Total stellar mass based on the K-band luminosity and the K-band mass-to-light ratios. (7) Star formation rate computed from the *IRAS* 60 μm and 100 μm flux, details are given in Section 3.3. (8) Morphological type, taken from NED. (9) Virial radius of the galaxies, estimated from the maximum rotation velocity. (10) Total *XMM-Newton* exposure time.

The observed X-ray emission from spiral galaxies consists of multiple components: (1) In addition to LMXBs (Gilfanov 2004), bright high-mass X-ray binaries (HMXBs), associated with star-formation, are located in the star-forming regions (Grimm et al. 2003); (2) Also an important contributor to the X-ray flux is the collective emission of faint compact X-ray sources, which contribute to the unresolved, diffuse component. The population of ABs and CVs follow the stellar light distribution (Revnivtsev et al. 2008), while the emission from young stars and young stellar objects is proportional with the star-formation rates of the host galaxy (Bogdán & Gilfanov 2011b). (3) Additionally, spiral galaxies host at least moderate amounts of ionized gas with sub-keV temperatures (Bogdán & Gilfanov 2011b). These components, enumerated above, provide the bulk of the observed emission within the optical extent of spiral galaxies and are very difficult to model accurately as an integrated component to detect the faint outer corona projected onto this complex region. Therefore, to probe the structure formation models, the hot X-ray coronae must be explored *beyond the optical extent* of spiral galaxies.

The primary goals of the present paper are twofold. First, we aim to detect and characterize the hot X-ray coronae beyond the optical disks of two massive spiral galaxies, NGC1961 and NGC6753, based on moderately deep *XMM-Newton* X-ray observations. Second, we aim to confront the observed physical properties of the X-ray coronae with those predicted by modern structure formation models.

The first analytic analysis of galaxy formation in the cold dark matter cosmogony was presented by White & Rees (1991), who suggested that X-ray coronae around massive galaxies should be ubiquitous. For example, their calculations argued that a halo, characterized by 300 km s^{-1} circular velocity, would have an X-ray luminosity of $3 \times 10^{42} \text{ erg s}^{-1}$ and a gas temperature of about 0.3 keV. However, the luminosities predicted by White & Rees (1991) are too high, because they neglected gas ejection and assumed that the hot gas follows the dark matter distribution. The hydrodynamical simulations of Toft et al. (2002) predict X-ray coronae about two orders of magnitude fainter than the original White & Rees (1991) predictions. The lower predicted luminosities are due to the absence of efficient feedback, which resulted in very massive stellar components, consequently much less massive and less luminous X-ray coronae. Most recently, Crain et al. (2010) studied the prop-

erties of rotationally supported systems with an extensive simulation of disk-like galaxies. This simulation, carried out in a large cosmological volume, incorporates efficient feedback from supernovae that prevents the conversion of halo gas into stars. The supernova feedback also alters the hot gas entropy profile by ejecting a fraction of the baryons to larger radii, and by preferentially ejecting the lowest entropy gas to suppress the central density profile.

The paper is structured as follows. In Section 2 we describe the previously available sample of spiral galaxies and introduce the presently studied NGC1961 and NGC6753. In Section 3 we describe the reduction of the X-ray and infrared data. The results, namely images, surface brightness profiles, and spectra, are presented in Section 4. The observed characteristics of the X-ray coronae are confronted with structure formation simulations in Section 5. We discuss our results in Section 6. We summarize in Section 7.

2. PREVIOUS OBSERVATIONS AND THE PRESENT SAMPLE OF SPIRAL GALAXIES

2.1. Previous observations of spiral galaxies

Prior to the *XMM-Newton* observations of NGC1961 and NGC6753, the data available for studying the extended X-ray coronae of spiral galaxies was very scarce for the following three reasons. First, most studied spiral galaxies have stellar masses of $M_* \lesssim 3 \times 10^{11} M_\odot$, implying rather faint X-ray coronae beyond their optical extent (Section 5.2). Therefore, the predicted faint X-ray coronae could not be detected: only upper limits are obtained, which means that the gaseous emission cannot be characterized. Examples for such spiral galaxies are those studied by Benson et al. (2000) based on *ROSAT* PSPC data, or the galaxies investigated by Rasmussen et al. (2009) based on *Chandra* observations. Second, most galaxies with detected X-ray coronae are *not normal* spiral galaxies, but they are either starburst/post starburst systems, active galactic nuclei (AGN), or spirals whose cold interstellar media have been heated and sometimes stripped by the interaction with the intracluster gas. Therefore, the starburst galaxies, including the famous M82 and NGC253, studied by Strickland et al. (2004a), or the galaxies located in rich cluster environment in the Sun et al. (2007) sample cannot be used to probe structure formation models. Third, the extra-planar X-ray emission detected in a number of normal, edge-on spiral galaxies is not extended to large radii but lies close to the disk (e.g. Wang 2005). The extraplanar X-ray emission in these spirals is not likely

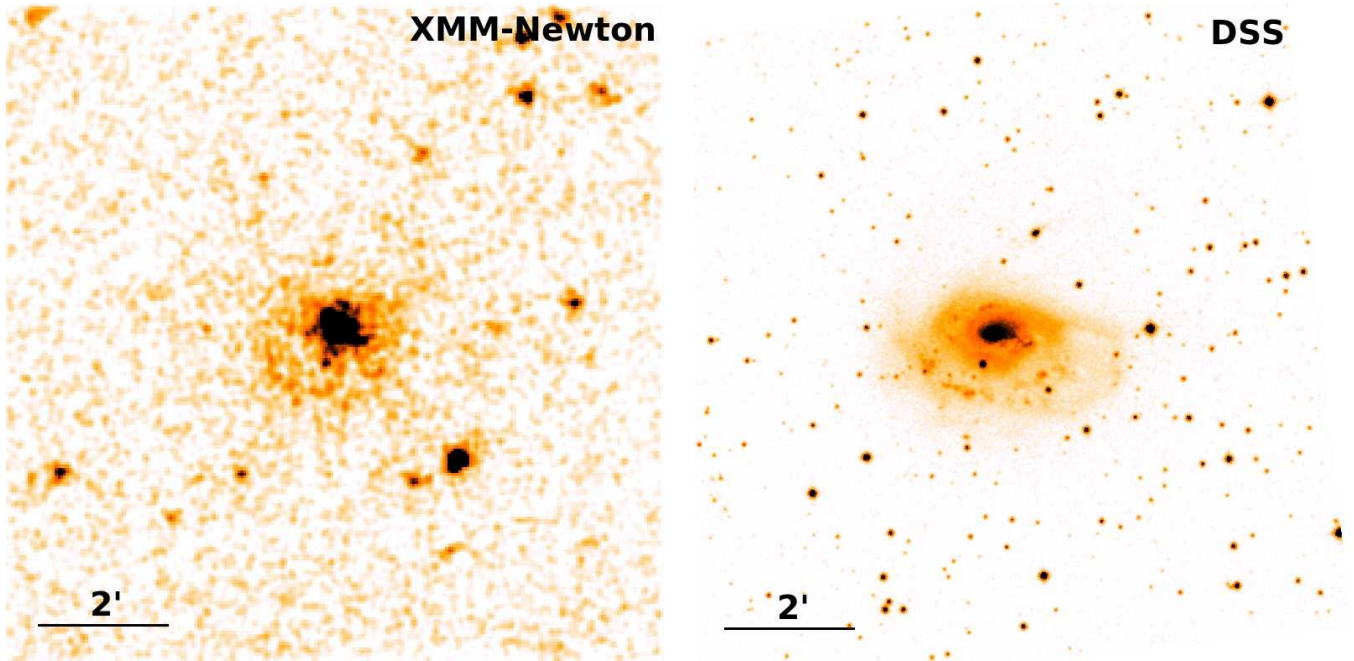


FIG. 1.— *Left*: 0.3–2 keV band raw *XMM-Newton* image of a $10' \times 10'$ region (162×162 kpc) around NGC1961. The net exposure time of the galaxy after flare filtering is 31.0, 34.1, and 21.3 ks for MOS1, MOS2, and PN, respectively. The bright X-ray sources beyond the optical radius are cosmic X-ray background sources. *Right*: DSS R-band image of the same region. The somewhat disturbed morphology may be the result of a recent minor merger (Combes et al. 2009).

that arising from an extended corona of infalling gas, but it is most likely a supernova (SN) driven outflow, as discussed by David et al. (2006) for low luminosity early-type galaxies and as observed in the bulge of M31 (Li & Wang 2007; Bogdán & Gilfanov 2008). Indeed, detailed studies of the extraplanar emission demonstrate that it is confined to within 10 kpc around NGC5775 (Li et al. 2008) and 23 kpc around M104 (Li et al. 2011), and can be interpreted as gas driven up from the disk.

The first luminous X-ray coronae around massive spiral galaxies have only recently been detected. Most recently, Bogdán et al. (2013) studied the massive spiral galaxy NGC266 based on a pointed *ROSAT* observation, and detected a luminous X-ray corona extending to at least 70 kpc. Adopting realistic gas temperatures and abundances, Bogdán et al. (2013) estimated that in the $(0.05 - 0.15)r_{200}$ region (where r_{200} is the virial radius) the bolometric X-ray luminosity of the hot gas is $(4.3 \pm 0.8) \times 10^{40}$ erg s $^{-1}$. Based on a 130 ks *Chandra* observation of NGC1961, Anderson et al. (2011) detected a luminous X-ray corona with the hot gas extending to about 40 kpc. They measured the spectrum of the integrated emission within 40 kpc to be $kT = 0.60^{+0.10}_{-0.09}$ keV temperature consistent with the expectations for a hot corona. However, the relatively few detected counts did not allow the measurement of the elemental abundances. Using *XMM-Newton* observations, Dai et al. (2011) reported the presence of a hot gaseous corona out to 80 kpc from the center of UGC12591, a rapidly rotating S0/a galaxy. The spectral properties of the gas were measured in the central ~ 24 kpc region of the galaxy, resulting in a best-fit temperature of $kT = 0.60 \pm 0.03$ keV.

2.2. Spiral galaxies analyzed in this paper

To detect and characterize hot X-ray coronae with present-day X-ray telescopes, the targeted galaxies must fulfill the following three criteria. First, the selected spiral galaxies must be massive. More massive galaxies are predicted to have more luminous X-ray coronae, thereby facilitating detections with high signal-to-noise ratios. Second, relatively relaxed galaxies are required in a “clean” environment, that is they should not be starburst systems, should not be undergoing an interaction or merger, should not host a significant AGN, and should not be located in a rich galaxy cluster. Finally, the radial range of 25–100 kpc should fit in the *XMM-Newton* field-of-view (FOV). The galaxies, NGC1961 and NGC6753 fulfill all these criteria. They are fairly massive ($M_{\star} > 3 \times 10^{11} M_{\odot}$), are quiescent, and are located in sufficiently distant poor galaxy groups (Fouque et al. 1992). Thus, NGC1961 and NGC6753 are excellent targets to test galaxy formation scenarios. Their major physical properties are listed in Table 1.

To estimate the virial mass (M_{200}) of the sample galaxies, we use the baryonic Tully-Fisher relation for the cold dark matter cosmogony, $M_{200} \propto V_{\max}^{3.23}$, where V_{\max} is the maximum rotational velocity of the galaxies. The V_{\max} values are taken from the HyperLeda¹ catalog (Paturel et al. 2003), which gives $V_{\max} = 447.9 \pm 14.6$ km s $^{-1}$ for NGC1961 and $V_{\max} = 395.0 \pm 21.1$ km s $^{-1}$ for NGC6753. Using results of numerical simulations (Navarro et al. 1997, Vogelsberger et al., in prep.), we estimate virial masses of $\sim 1.2 \times 10^{13} M_{\odot}$ and $\sim 1.0 \times 10^{13} M_{\odot}$ for NGC1961 and NGC6753, respec-

¹ <http://leda.univ-lyon1.fr>

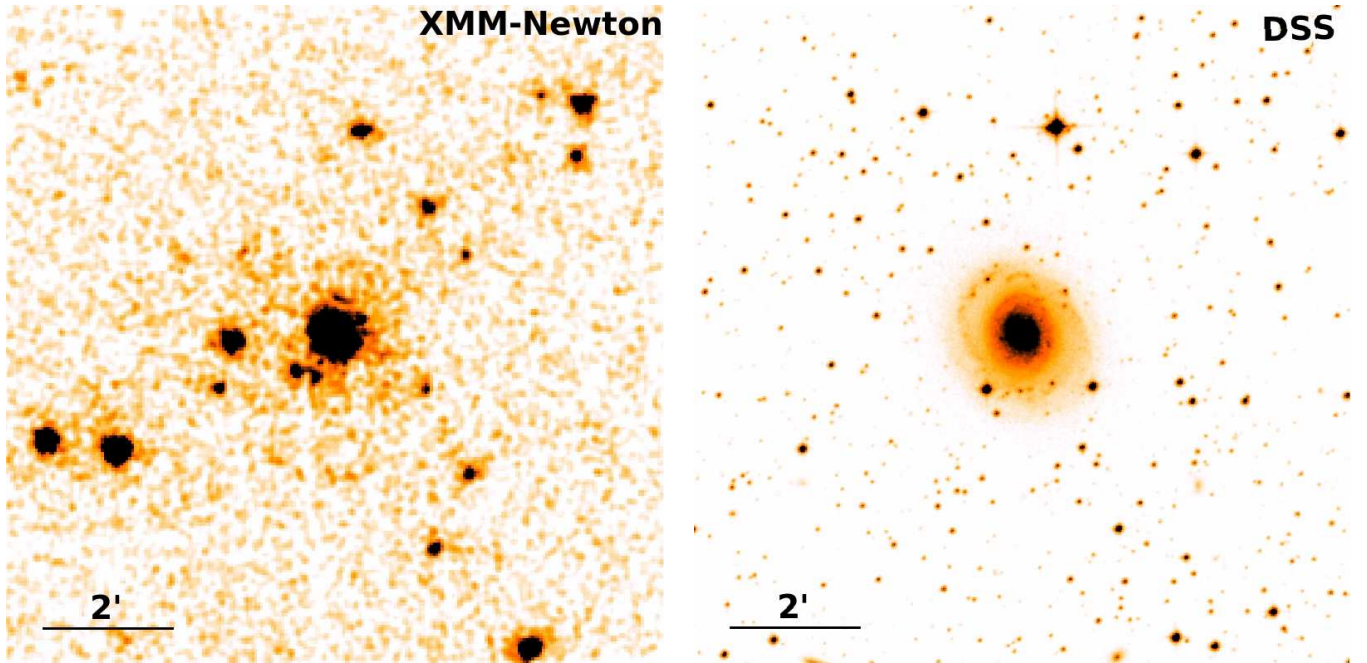


FIG. 2.— *Left*: 0.3 – 2 keV band raw *XMM-Newton* image of a $10' \times 10'$ region (127×127 kpc) around NGC6753. The net exposure time of the galaxy after flare filtering is 58.7, 59.2, and 27.9 ks for MOS1, MOS2, and PN, respectively. The bright X-ray sources beyond the optical radius are cosmic X-ray background sources. *Right*: DSS R-band image of the same region. The symmetrical morphology of the galaxy indicates its undisturbed nature.

TABLE 2
THE LIST OF ANALYZED *XMM-Newton* OBSERVATIONS.

Galaxy	<i>XMM-Newton</i> Obs ID	Centre coordinates	MOS1 clean exposure time (ks)	MOS2 clean exposure time (ks)	PN clean exposure time (ks)	Observation Date
NGC1961	0673170101	05h42m04.60s +69d22'42.0"	16.0	19.1	12.7	2011 Aug 31
NGC1961	0673170301	05h42m04.60s +69d22'42.0"	15.0	15.0	8.6	2011 Sep 14
NGC6753	0673170201	19h11m23.60s –57d02'58.0"	58.7	59.2	27.9	2012 Apr 21

tively. From the virial masses we compute the virial radii (r_{200}) of the galaxies using:

$$M_{200} = 200\rho_{\text{crit}}\frac{4\pi}{3}r_{200}^3, \quad (1)$$

where ρ_{crit} is the critical density of the Universe. We thus estimate that the virial radii of NGC1961 and NGC6753 are $r_{200} \sim 470$ kpc and $r_{200} \sim 440$ kpc, respectively.

We emphasize that the applied method serves as a crude estimate of M_{200} (hence r_{200}). Precisely determining these quantities is a rather convoluted task, which is beyond the scope of this paper. We note that the main application of M_{200} is to determine r_{200} . However, as is clear from equation (1), r_{200} is relatively weakly dependent on the virial mass, hence it is much less affected by the uncertainties associated with the determination of M_{200} . Thus, the conclusions of this paper remain completely valid, even if the “real” virial mass/radius is somewhat different than the quoted values.

3. DATA REDUCTION

3.1. X-ray observations

NGC1961 was observed with the European Photon Imaging Camera (EPIC) aboard *XMM-Newton* in two observations (ObsID: 0673170101, 0673170301) for a total of 73.7 ks, whereas NGC6753 was observed in one pointing (ObsID: 0673170201) for 73.9 ks. Further details about the observations are listed in Table 2.

Since the main steps of the data reduction are identical with those outlined in Bourdin & Mazzotta (2008), here we only emphasize the major points. As a first step, we processed the event lists using the *XMM* Science Analysis System (SAS) version 10.0 and Current Calibration Files (CCF). We further identified and removed the flare contaminated time periods for each observation and camera separately, employing a two-step filtering of the high energy (10 – 12 keV) and softer energy events (1 – 5 keV). The clean exposure times are 30 – 80% of the original exposures. To increase the signal-to-noise ratio, we combined the data from the EPIC MOS and EPIC PN instruments, and also merged the two pointings of NGC1961. Since the goal of our study is to characterize the diffuse emission, bright point sources were identified using the combined EPIC PN and MOS data. To do so, we selected the PSF smeared point sources up to a radius

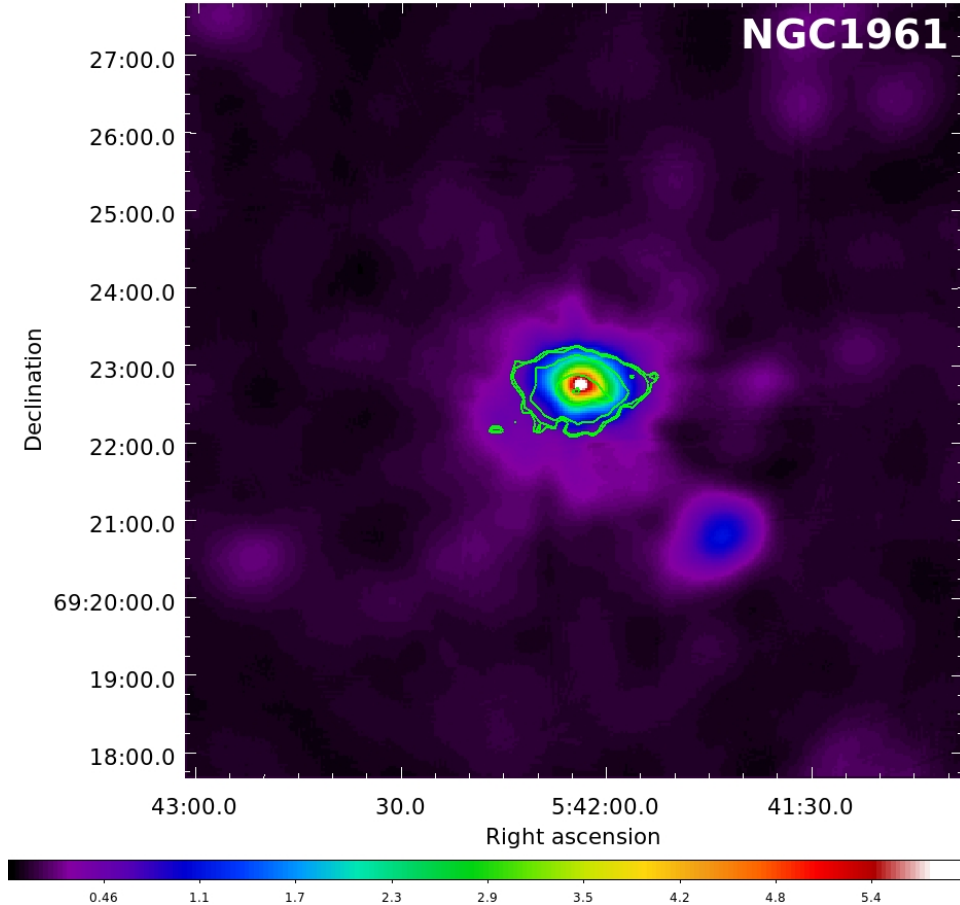


FIG. 3.— Denoised surface brightness image of NGC1961 based on the combined *XMM-Newton* EPIC datasets. The side length of the image is $10'$, which corresponds to 162.3 kpc at the distance of the galaxy. The image reveals large-scale extended emission surrounding the galaxy originating from the hot X-ray gas. Note that point sources are not excluded from the image. The distribution of the hot gas is fairly symmetric. To illustrate the extent and distribution of the stellar light, the K-band intensity levels are overplotted. The contour levels are logarithmically scaled from $2 \times 10^7 L_{K,\odot} \text{ arcsec}^{-2}$ to $5 \times 10^8 L_{K,\odot} \text{ arcsec}^{-2}$. Within the outermost contour level, the enclosed light is $\sim 3.2 \times 10^{11} L_{K,\odot}$, which is $\sim 76\%$ of the total K-band luminosity of NGC1961.

where their surface brightness reaches the background noise fluctuation. These radii are derived from the analysis of wavelet denoised images of the field of view using the Source Extractor software (Bertin & Arnouts 1996). With typical radii in the range of $10 - 30''$, the detected point sources are masked out in the further analysis of the diffuse emission.

Images and surface brightness profiles of the diffuse emission are presented in Figures 3, 4, 5, and 6. All of these are corrected for effective areas and background noise models. Spatially and spectrally sampled, the background model consists of (i) the cosmic-ray induced particle background, (ii) the expected out-of-time count rate, (iii) a residual emission associated with soft protons (iv) a vignettted, extragalactic power-law component, (v) a vignettted two-phase thermal plasma model designed to account for emission from the Milky Way. Derived from “closed-filter” data sets, the cosmic-ray induced particle background includes spatially variable continua and fluorescence lines for each detector CCD, as detailed in Bourdin et al. (2013). The out-of-time count rate is fixed in each energy band to 6.3% of all photon counts registered along the CCD columns.

A soft proton excess was detected and modelled as a power-law in the case of NGC1961. The extragalactic power-law index is fixed to 1.42 (see e.g. Lumb et al. 2002), while the Galactic foregrounds are modelled by the sum of two thermal bremsstrahlung spectra with Solar metal abundances ($kT_1 = 0.099$ keV and $kT_2 = 0.248$ keV), accounting for the Galactic transabsorption emission (Kuntz & Snowden 2000). All of these components were first normalized using a spectral fit to the source data in an annulus with $10' - 15'$ radii, and then individually rescaled within each image pixel and energy bin using the appropriate vignetting factors. The accuracy of the model can be seen in Figure 7.

Since accurate background subtraction is crucial in our study, we checked the accuracy of the method discussed above by two means. First, we accounted for the background components using the EPIC “blank sky” files (Carter & Read 2007). These background files were tailor made for our observations, that is they were selected to approximately match the galactic foreground absorption values of NGC1961 and NGC6753 and the revolution number of the *XMM-Newton* observations. To match the observed count rates, we re-normalized the background

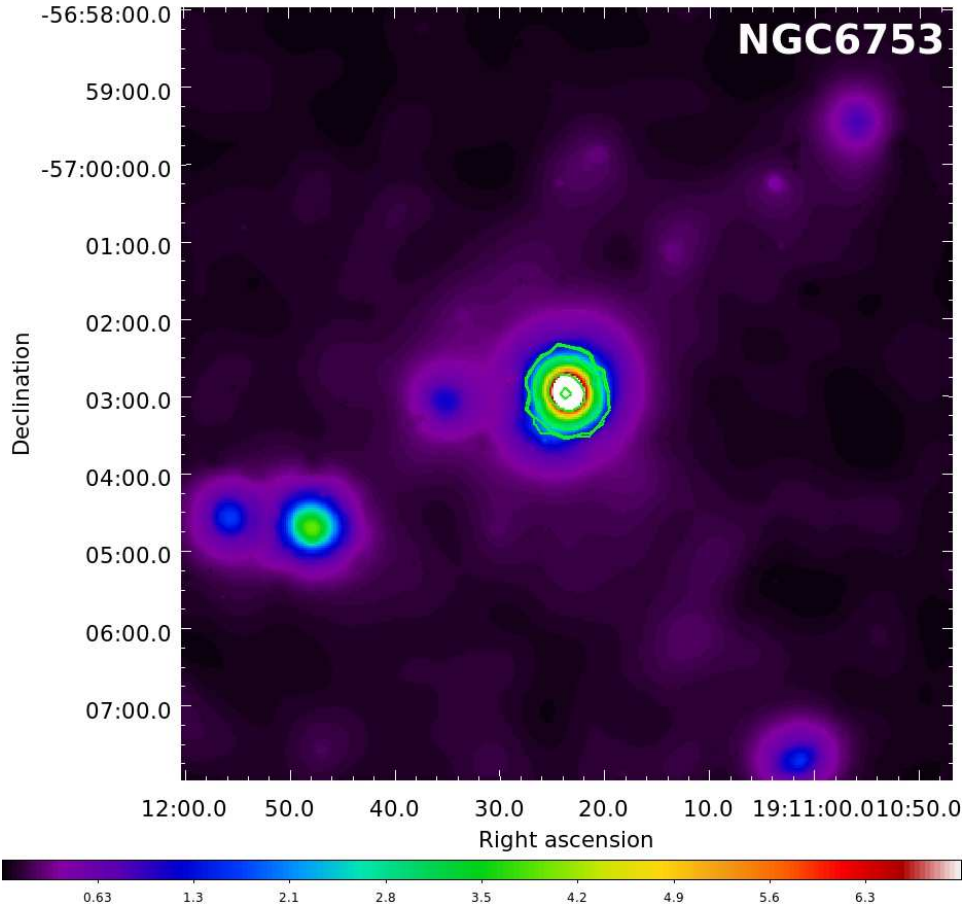


FIG. 4.— Denoised surface brightness image of NGC6753 based on the combined *XMM-Newton* EPIC datasets. The side length of the image is $10'$, which corresponds to 126.7 kpc at the distance of the galaxy. The diffuse X-ray emission, whose spectral signature is that of hot gas, extends beyond the optical radius of the galaxy. Note that point sources are not excluded from the image. The overplotted K-band intensity levels demonstrate the distribution and extent of the stellar light. The contour levels are logarithmically scaled from $2 \times 10^7 \text{ L}_{K, \odot} \text{ arcsec}^{-2}$ to $5 \times 10^8 \text{ L}_{K, \odot} \text{ arcsec}^{-2}$. Within the outermost contour level the enclosed light is $\sim 2.8 \times 10^{11} \text{ L}_{K, \odot}$, which is $\sim 88\%$ of the total K-band luminosity of the galaxy.

files using the 11 – 12 keV band count rates, where the effective area of *XMM-Newton* is negligible. Second, we analyzed the publicly available *Chandra* observations of NGC1961 (ObsId: 10528-10533). To reduce the data and subtract the background components, we followed the method described in Bogdán & Gilfanov (2008). Using these two different methods, we constructed X-ray surface brightness distributions and extracted X-ray energy spectra of the studied galaxies (only NGC1961 for *Chandra*). These were compared with the profiles and spectra obtained from our standard background subtraction method, which models all background components. The resulting profiles agree with each other within statistical uncertainties at all radii, moreover the obtained best-fit parameters of the spectra also agree within the 1σ uncertainties. Since all three background subtraction methods result in comparable profiles and spectra, it implies that our background subtraction method is robust and accurate.

3.2. Near-infrared observations

To trace the stellar light of NGC1961 and NGC6753, we rely on the K-band data of the Two-Micron All

Sky Survey (2MASS) Large Galaxy Atlas (Jarrett et al. 2003). The observed background subtracted K-band counts (S) are converted to physical units using

$$m_K = \text{KMAGZP} - 2.5 \log S, \quad (2)$$

where m_K is the apparent K-band magnitude, and KMAGZP is the zero point magnitude given in the image header. The derived m_K is converted to an absolute magnitude and luminosity assuming that the absolute K-band magnitude of the Sun is $M_{K, \odot} = 3.28$ mag. The total K-band luminosities of NGC1961 and NGC6753 are $5.4 \times 10^{11} \text{ L}_{K, \odot}$ and $3.9 \times 10^{11} \text{ L}_{K, \odot}$, respectively.

We compute the total stellar mass of NGC1961 and NGC6753 from their K-band luminosities and from the K-band mass-to-light ratios (Table 1). The mass-to-light ratios are derived from the $B - V$ color indices and results of galaxy evolution modeling (Bell et al. 2003). The mass-to-light ratios are $0.78 \text{ M}_{\odot} / \text{L}_{K, \odot}$ for NGC1961 and $0.81 \text{ M}_{\odot} / \text{L}_{K, \odot}$ for NGC6753, hence their total stellar masses are $4.2 \times 10^{11} \text{ M}_{\odot}$ and $3.2 \times 10^{11} \text{ M}_{\odot}$, respectively.

While the uncertainties associated with the K-band photometry are $\lesssim 3\%$, the mass-to-light ratios obtained

from the $B-V$ color indices and the Bell et al. (2003) relation employ a number of assumptions and are affected by notable systematic uncertainties. The most important assumption is the applied stellar initial mass function, while the systematic uncertainties are dominated by the effects of dust and starbursts, which may result in $\sim 25\%$ uncertainty. The importance and significance of various assumptions and uncertainties is discussed in full particulars in Bell et al. (2003).

3.3. Far-infrared observations

We compute the star-formation rates (SFRs) of NGC1961 and NGC6753 based on their far-infrared emission observed by the *Infrared Astronomical Satellite* (*IRAS*), and applying the relation described by Kennicutt (1998):

$$\text{SFR}_{\text{IR}} (\text{M}_{\odot} \text{ yr}^{-1}) = 4.5 \times 10^{-44} L_{\text{IR}} (\text{erg s}^{-1}), \quad (3)$$

where L_{IR} is the total infrared luminosity in the $8 - 1000 \mu\text{m}$ regime. To obtain the total infrared luminosity, we follow the procedure of Meurer et al. (1999). The total far-infrared flux (F_{FIR}) in the $40 - 120 \mu\text{m}$ range (Helou et al. 1988) is

$$F_{\text{FIR}} = 1.26 \times 10^{-11} (2.58 F_{60\mu\text{m}} + F_{100\mu\text{m}}), \quad (4)$$

where $F_{60\mu\text{m}}$ and $F_{100\mu\text{m}}$ are the *IRAS* fluxes at $60 \mu\text{m}$ and $100 \mu\text{m}$ (Sanders et al. 2003). To convert the flux to a luminosity, we use $L_{\text{FIR}} = 4\pi D_L^2 F_{\text{FIR}}$, where D_L^2 is the luminosity distance of the galaxy. Since the Kennicutt (1998) relation refers to the total infrared luminosity, we convert L_{FIR} to L_{IR} applying the formula of Calzetti et al. (2000):

$$L_{\text{IR}} \sim 1.75 L_{\text{FIR}}. \quad (5)$$

Although this conversion refers to the $1 - 1000 \mu\text{m}$ band and not to the $8 - 1000 \mu\text{m}$ band, the contribution from the $1 - 8 \mu\text{m}$ range is not expected to exceed the few per cent level (Calzetti et al. 2000), yielding slightly overestimated SFRs. We thus obtain SFRs of $15.5 \text{ M}_{\odot} \text{ yr}^{-1}$ in NGC1961 and $11.8 \text{ M}_{\odot} \text{ yr}^{-1}$ in NGC6753, implying moderate ongoing star-formation.

4. RESULTS

To detect and characterize the physical properties of the hot X-ray coronae around NGC1961 and NGC6753, we employ three different techniques. First, we produce surface brightness images in the $0.3 - 2 \text{ keV}$ band to map the spatial distribution of the diffuse X-ray emission around the galaxies. Second, we build X-ray surface brightness profiles, which we compare with the stellar light distribution. Third, to measure the physical properties of the coronal X-ray emission, we extract the X-ray energy spectra.

4.1. Images

To map the large-scale spatial distribution of the diffuse emission around NGC1961 and NGC6753, we construct surface brightness images. The images are produced in the $0.3 - 2 \text{ keV}$ energy band. This particular choice of the energy range is advantageous because 1) the hot X-ray gas is predicted to have sub-keV temperatures (Section 5.4), hence the bulk of its emission is produced

in the soft band, 2) the effective area of *XMM-Newton* detectors is the highest, and 3) the level of instrumental and cosmic X-ray background is fairly low in the $0.3 - 2 \text{ keV}$ band.

In Figures 1 and 2 we show the unprocessed $0.3 - 2 \text{ keV}$ band EPIC MOS images of the central $10' \times 10'$ regions of NGC1961 and NGC6753, respectively. The X-ray images are compared with optical images from the Digitized Sky Survey (DSS). An apparent X-ray glow is associated with both galaxies within their optical extent. As discussed in Section 1, this X-ray emission originates from the population of resolved and unresolved discrete sources, while truly diffuse gaseous emission also contributes. However, in the unprocessed images, the diffuse X-ray emission cannot be identified beyond the optical extent of the galaxies, due to the faint nature of the hot X-ray coronae and the relatively high background level.

In order to better visualize the faint X-ray coronae of the sample galaxies beyond their optical extent, we produce “denoised” surface brightness maps of the photon images following Starck et al. (2009). The images are background subtracted and vignetting corrected. To facilitate the comparison with the stellar light distribution, logarithmically-scaled contour levels of the K-band light are overplotted.

The “denoised” $0.3 - 2 \text{ keV}$ band X-ray images suggest the presence of extended diffuse emission around both NGC1961 (Figure 3) and NGC6753 (Figure 4), whose extents significantly exceed those of the stellar light. Whereas the dominant fraction of the optical light is confined to within $\sim 1.5'$, the diffuse X-ray emission appears to extend to several arcminutes in both galaxies. As discussed in Section 4.3, the spectral signature of this emission is that of hot gas. The morphology of the X-ray emission is fairly symmetric, thereby hinting that the hot gas resides in hydrostatic equilibrium in the dark matter halos of NGC1961 and NGC6753. The characteristics of these X-ray coronae are further discussed in Sections 4.2 and 4.3.

4.2. Profiles

To further study the spatial distribution and the morphology of the diffuse X-ray emission around NGC1961 and NGC6753, we construct X-ray surface brightness profiles. The profiles are extracted from the $0.3 - 2 \text{ keV}$ energy band using the combined *XMM-Newton* EPIC data. From the profiles all background components are subtracted, vignetting correction is applied, and bright resolved point sources are masked out.

To extract the X-ray surface brightness profiles, we employ circular annuli centered on the optical center of each galaxy. The distribution of the X-ray light is compared with the stellar light distribution, which is measured with the 2MASS K-band images. The K-band light profiles are extracted using the same circular annuli, moreover the locations of X-ray sources are masked out from the K-band images, along with the population of bright foreground stars. Note that the uncertainties in the X-ray surface brightness are of a statistical nature, but at large offsets the systematic uncertainties dominate. The profiles, depicted in Figure 5, confirm that the diffuse X-ray emission extends well beyond the optical radii for NGC1961 and NGC6753. Whereas the stellar light is confined to within $20 - 25 \text{ kpc}$ ($\sim 1.5'$), the diffuse X-ray

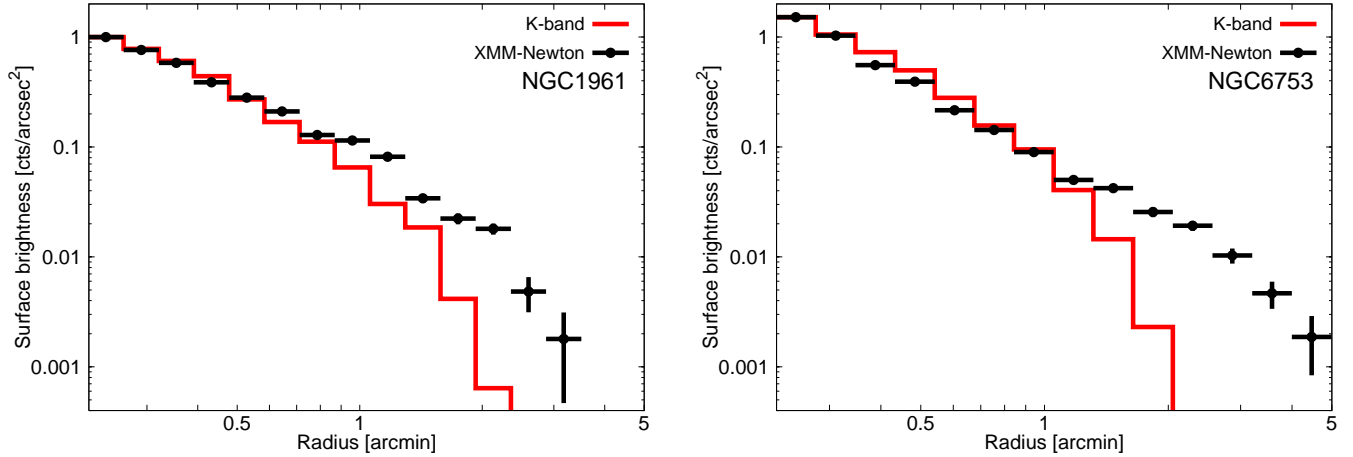


FIG. 5.— Surface brightness distribution of the 0.3 – 2 keV band diffuse X-ray emission for NGC1961 (left panel) and NGC6753 (right panel) obtained from the combined data of *XMM-Newton* EPIC PN and EPIC MOS cameras. To construct the profiles, we used circular annuli centered on the optical centroid of each galaxy. Vignetting correction is applied and all background components are subtracted. The X-ray light distributions are compared with the K-band light profiles. The K-band profiles are normalized to match the level of X-ray emission in the innermost bins.

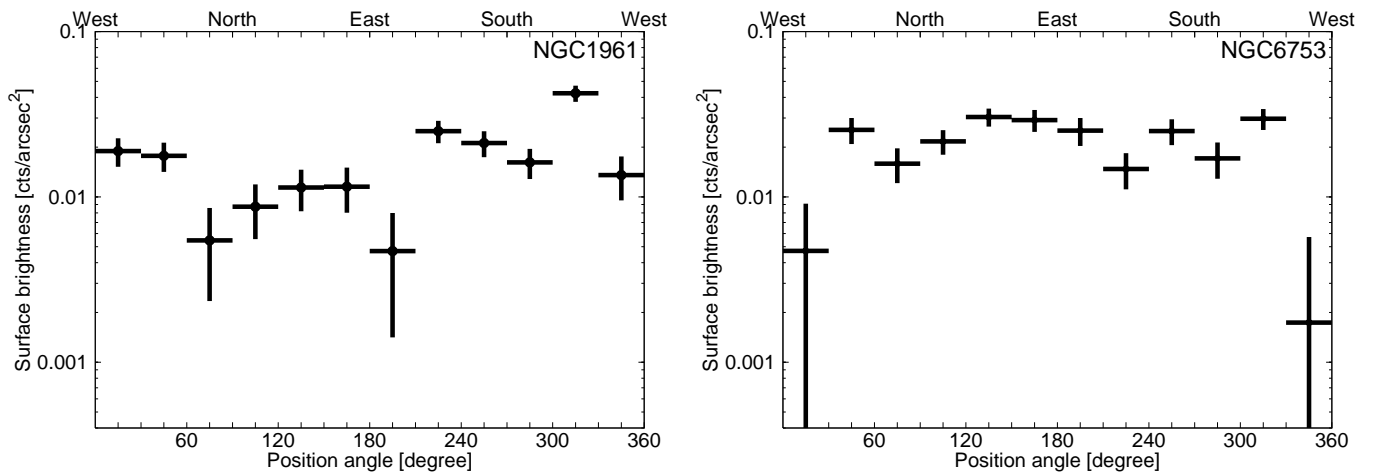


FIG. 6.— Surface brightness distribution of the 0.3 – 2 keV band diffuse X-ray emission for NGC1961 (left panel) and NGC6753 (right panel) obtained from the combined data of *XMM-Newton* EPIC PN and EPIC MOS cameras. The profiles are obtained from circular wedges, whose inner and outer radii are $1.25' - 3'$ for both galaxies. Vignetting correction is applied and the background components are subtracted. As shown in the upper x-axis, 90° corresponds to north and 180° corresponds to east.

emission is detected out to ~ 57 kpc ($3.5'$) in NGC1961 and ~ 63 kpc ($5'$) in NGC6753. This implies that the diffuse X-ray emission at large radii cannot be associated with the stellar body of the host galaxies. Interestingly, the observed surface brightness distribution of NGC6753 is flatter than that obtained for NGC1961, implying that the emission may extend beyond $\sim 5'$. However, beyond this radius the surface brightness drops rapidly and – due to the rather high instrumental background level of *XMM-Newton* – statistically significant emission cannot be detected. To explore the hot X-ray corona of NGC6753 beyond $\sim 5'$, deep *Chandra* observations are desirable.

In the “denoised” images, the diffuse emission appears to be fairly symmetric. To further probe the spatial distribution of the X-ray emission, we produce X-ray surface brightness profiles using circular wedges centered on

the centroid of each galaxy. Since we aim to probe the surface brightness beyond the optical extent, the wedges are extracted from annuli with radii of $1.25' - 3'$ for both galaxies. Since the stellar light is negligible in this region, we do not plot the level of renormalized K-band light. As before, the uncertainties are of a purely statistical nature. The circular profiles, shown in Figure 6, demonstrate that the hot X-ray gas has a fairly uniform distribution around both galaxies at every position angle. The spatial distributions are morphologically consistent with warm gas residing in hydrostatic equilibrium in the potential well of the galaxies, and are morphologically inconsistent with a starburst or AGN driven bipolar outflow.

4.3. Spectra

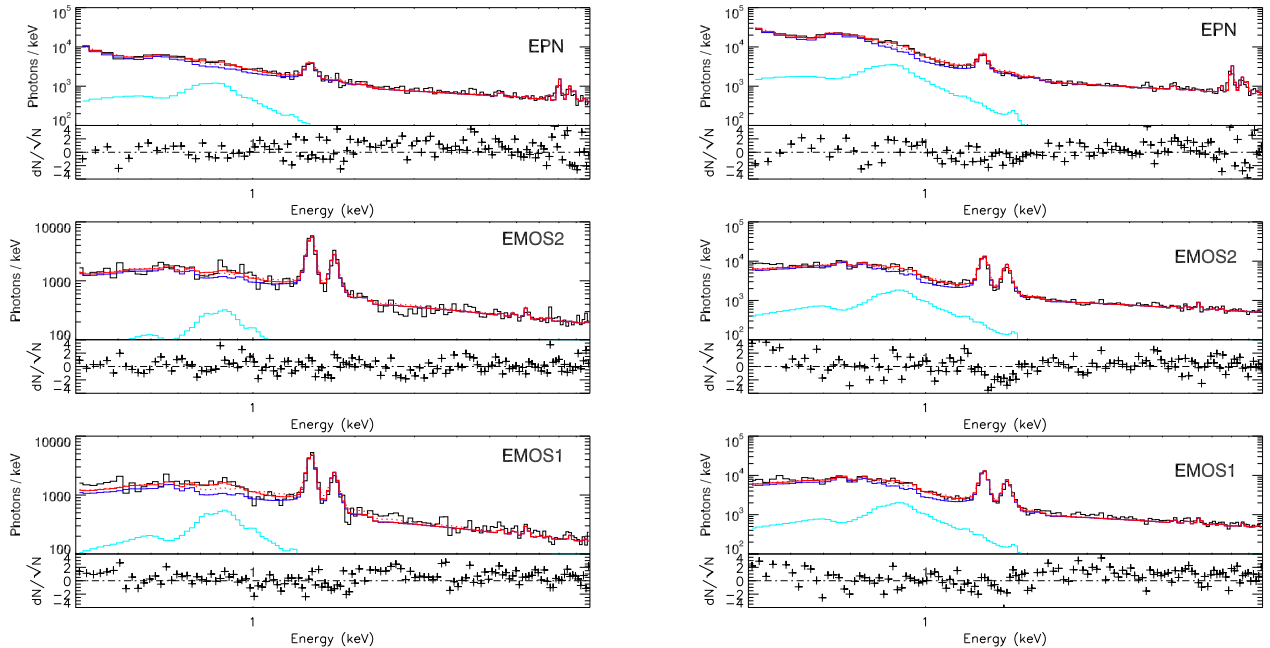


FIG. 7.— X-ray energy spectra of NGC1961 (left panel) and NGC6753 (right panel) in the 0.3 – 10 keV band obtained from the *XMM-Newton* EPIC PN (top panel) MOS1 (middle) and MOS2 (bottom) cameras. The depicted spectra are extracted for the $(0.05 - 0.15)r_{200}$ radial range. The contribution of bright point sources are removed. The spectra are fit with an absorbed thermal plasma emission model. The black lines show the data set and the red lines represent the overall fit. Dark blue shows the overall background components, whereas light blue is the emission associated with the thermal spectrum. The bottom panels of each plot show the residuals with respect to the best-fit thermal model.

4.3.1. Observed parameters in the $(0.05 - 0.15)r_{200}$ region

To study the nature and physical properties of the diffuse X-ray emission around NGC1961 and NGC6753, we extract X-ray energy spectra. As we aim to probe the hot gas beyond the optical radii, we exclude the central regions of the galaxies. To facilitate the comparison with structure formation simulations, we convert all radial distances to r_{200} units (Section 2.2). For both galaxies, we extract spectra from circular annuli with $(0.05 - 0.15)r_{200}$, which correspond to the physical distances of 23.5 – 70.5 kpc for NGC1961 and 22.0 – 66.0 kpc for NGC6753.

In Figure 7 we show the EPIC PN and EPIC MOS spectra for NGC1961 and NGC6753, which demonstrate the presence of a soft X-ray emitting component at energies below 2 keV. Within the studied region we detect 1778 and 4858 net counts from NGC1961 and NGC6753. Defining the signal-to-noise ratio as $\text{SNR} = (C_s/C_B^{0.5})$, where C_s is the number of net counts and C_B is the number of background counts, we obtain $\text{SNR}_{\text{NGC1961}} = 13.1$ and $\text{SNR}_{\text{NGC6753}} = 22.3$ for NGC1961 and NGC6753, respectively. To describe the soft X-ray emitting component, we employ an absorbed thermal plasma model (WABS*APEC in XSPEC). When fitting the spectra, the column density is fixed at the Galactic value (Dickey & Lockman 1990) and the abundance is left free to vary. For spectral fitting the abundance table of Grevesse & Sauval (1998) is used. The thermal components describe the spectra with reduced $\chi^2 = 1.27$ for NGC1961 and reduced $\chi^2 = 1.79$ for NGC6753. These spectra indicate that the diffuse X-ray emission originates from hot gas. However, these fits are

formally not acceptable, which may be the result of the complex thermal and/or abundance structure of the hot gas or it could be an artifact caused by the insufficient energy resolution of the detectors.

Based on the best-fit spectra we measure the average parameters of the hot gas within the $(0.05 - 0.15)r_{200}$ region. For both NGC1961 and NGC6753, we obtained similar gas temperatures ($kT \sim 0.6 - 0.7$ keV) and sub-solar abundances (0.12 – 0.13 Solar). From the emission measure of the spectra ($\int n_e n_H dV$), we compute the average electron number density, the confined gas mass, and the average cooling time. As a caveat we mention that the emission measure and abundances of the thermal component are strongly anticorrelated (Section 6.3). To compute the hot gas mass, we assumed a spherically symmetric gas distribution, constant density, and a volume filling factor of unity. Given the volume of the studied regions, we obtained hot gas masses of about $\sim 10^{10} M_\odot$ and electron number densities of $(3.5 - 4) \times 10^{-4} \text{ cm}^{-3}$ for both galaxies. The cooling time of the gas is computed from $t_{\text{cool}} = (3kT)/(n_e \Lambda(T))$, where $\Lambda(T)$ is the cooling function at the best-fit temperature and abundance. For both NGC1961 and NGC6753 we obtain $t_{\text{cool}} \sim 50$ Gyrs, much longer than the Hubble-time. The uncertainties of the emission measure (and other quantities derived from its value) are estimated from the parameter covariance matrix by assuming a quadratic χ^2 distribution. The parameters of the warm gas are listed in Table 3.

From the best-fit spectra, we also compute the X-ray luminosity of the hot gas in the $(0.05 - 0.15)r_{200}$ radial bin. In the 0.5 – 2 keV band, we obtain absorbed luminosities of $L_{0.5-2\text{keV,abs}} = (2.0 \pm 0.6) \times 10^{40} \text{ erg s}^{-1}$ for NGC1961 and $L_{0.5-2\text{keV,abs}} = (2.5 \pm 0.4) \times 10^{40} \text{ erg s}^{-1}$.

TABLE 3
THE PARAMETERS OF THE EXTENDED HOT GASEOUS CORONAE AROUND NGC1961 AND NGC6753.

Galaxy	Radial range r_{200}	$\int n_e n_H dV$ cm^{-3}	kT keV	Abundance	M_{gas} M_{\odot}	n_e cm^{-3}	t_{cool} Gyr
NGC1961	0.05 – 0.15	$(5.2 \pm 1.5) \times 10^{63}$	$0.61^{+0.10}_{-0.13}$	0.12 ± 0.03	$(1.2 \pm 0.2) \times 10^{10}$	$(3.5 \pm 0.5) \times 10^{-4}$	45 ± 6
NGC6753	0.05 – 0.15	$(5.3 \pm 0.8) \times 10^{63}$	$0.69^{+0.06}_{-0.07}$	0.13 ± 0.02	$(1.1 \pm 0.1) \times 10^{10}$	$(3.9 \pm 0.3) \times 10^{-4}$	51 ± 4
NGC1961	0.15 – 0.30	$< 1.2 \times 10^{63}$	0.6^{\dagger}	0.12^{\dagger}	$< 1.6 \times 10^{10}$	$< 6.4 \times 10^{-5}$	> 258
NGC6753	0.15 – 0.30	$< 9.6 \times 10^{62}$	0.6^{\dagger}	0.13^{\dagger}	$< 1.3 \times 10^{10}$	$< 6.2 \times 10^{-5}$	> 266

\dagger These parameters were fixed at the given value.

TABLE 4
THE FLUX AND LUMINOSITY OF THE EXTENDED HOT GASEOUS CORONAE AROUND NGC1961 AND NGC6753.

Galaxy	Radial range r_{200}	$F_{0.5-2\text{keV,abs}}$ $\text{erg s}^{-1} \text{cm}^{-2}$	$L_{0.5-2\text{keV,abs}}$ erg s^{-1}	$L_{0.5-2\text{keV,unabs}}$ erg s^{-1}	L_{bol} erg s^{-1}
NGC1961	0.05 – 0.15	$(5.4 \pm 1.6) \times 10^{-14}$	$(2.0 \pm 0.6) \times 10^{40}$	$(2.8 \pm 0.8) \times 10^{40}$	$(5.8 \pm 1.7) \times 10^{40}$
NGC6753	0.05 – 0.15	$(1.1 \pm 0.2) \times 10^{-13}$	$(2.5 \pm 0.4) \times 10^{40}$	$(3.1 \pm 0.5) \times 10^{40}$	$(6.3 \pm 0.9) \times 10^{40}$
NGC1961	0.15 – 0.30	$< 1.3 \times 10^{-14}$	$< 4.8 \times 10^{39}$	$< 6.7 \times 10^{39}$	$< 1.4 \times 10^{40}$
NGC6753	0.15 – 0.30	$< 1.1 \times 10^{-14}$	$< 2.5 \times 10^{39}$	$< 3.1 \times 10^{39}$	$< 6.5 \times 10^{39}$

Using the Galactic column densities (Dickey & Lockman 1990), we convert these values to unabsorbed luminosities. Finally, we also derive the corresponding bolometric luminosities of the X-ray coronae, and we find $L_{\text{bol}} = (5.8 \pm 1.7) \times 10^{40} \text{ erg s}^{-1}$ and $L_{\text{bol}} = (6.3 \pm 0.9) \times 10^{40} \text{ erg s}^{-1}$ for NGC1961 and NGC6753, respectively. The obtained fluxes and luminosities are listed in Table 4.

4.3.2. Upper limits in the $(0.15 - 0.30)r_{200}$ region

In the $(0.15 - 0.30)r_{200}$ region, we do not detect a statistically significant X-ray emission above the background level in either NGC1961 or NGC6753. In the absence of hot gas detection beyond $\sim 0.15r_{200}$, we place upper limits on its physical parameters in the $(0.15 - 0.30)r_{200}$ region. This region is well within the *XMM-Newton* FOV, and corresponds to the radial range of 70.5 – 141.0 kpc for NGC1961 and 66.0 – 132.0 kpc for NGC6753. From the observed count rates within these regions, we derive 3σ upper limits using the EPIC PN data. To constrain the gas properties, we rely on the gas parameters observed within the $(0.05 - 0.15)r_{200}$ region. In particular, we assume the abundance of 0.12 Solar for NGC1961 and 0.13 Solar for NGC6753, and we adopt $kT = 0.6 \text{ keV}$ for both galaxies.

Using the appropriate response files, we derive upper limits on the emission measure, which we use to place upper limits on the confined gas mass, the electron number density, and the cooling time. Within the $(0.15 - 0.30)r_{200}$ region, the 3σ upper limit on the gas mass is $< 1.6 \times 10^{10} M_{\odot}$ and $< 1.3 \times 10^{10} M_{\odot}$ for NGC1961 and NGC6753, respectively. For the average electron number density, we derive $< 6.4 \times 10^{-5} \text{ cm}^{-3}$ in NGC1961 and $< 6.2 \times 10^{-5} \text{ cm}^{-3}$ in NGC6753. The cooling times for both galaxies are longer than 250 Gyrs, hence significantly exceed the Hubble-time, implying the quasi-static nature of the hot gas. The obtained upper limits are listed in Table 3.

Based on the upper limits on the emission measure, we also constrain the X-ray luminosities within the $(0.15 - 0.30)r_{200}$ region (Table 4). The upper limits

on the absorbed 0.5 – 2 keV band luminosities are $< 4.8 \times 10^{39} \text{ erg s}^{-1}$ and $< 2.5 \times 10^{39} \text{ erg s}^{-1}$ for NGC1961 and NGC6753, respectively. These values correspond to the bolometric luminosities of $< 1.4 \times 10^{40} \text{ erg s}^{-1}$ in NGC1961 and $< 6.5 \times 10^{39} \text{ erg s}^{-1}$ in NGC6753.

5. COMPARISON WITH NUMERICAL SIMULATIONS

5.1. Numerical codes

In this paper the observed properties of X-ray coronae around NGC1961 and NGC6753 are confronted with hydrodynamical simulations of structure formation. In particular, we probe the recently developed moving mesh code AREPO (Springel et al. 2010) and the traditional SPH-based code GADGET (Springel 2005). The codes and the methodology of the simulations are discussed in full particulars in Vogelsberger et al. (2012).

GADGET is a widely used and well tested SPH code, which simultaneously conserves energy and entropy despite the use of fully adaptive smoothing lengths (Springel & Hernquist 2002). The gravity calculation is split into short-range and long-range components, where the short-range forces are calculated with a hierarchical oct-tree algorithm (Barnes & Hut 1986; Hernquist 1987) and the long-range forces are evaluated with a particle mesh (PM) method (e.g. Hockney & Eastwood 1981). The simulations presented here are based on a default setting of the numerical SPH parameters (see Vogelsberger et al. 2012, for details). AREPO is a second-order accurate finite volume method that solves the Euler equations using piece-wise linear reconstruction and a calculation of hydrodynamical fluxes at each cell interface with an exact Riemann solver. The basic solution strategy of the code is that of the well-known MUSCL-Hancock scheme. AREPO employs an unstructured mesh based on a Voronoi tessellation using a set of mesh-generating points. This mesh is allowed to move freely as a function of time. In the simulations presented here, the motion of the mesh-generating points is tied to the hydrodynamical flow resulting in a quasi-Lagrangian character and makes the mesh automatically adaptive. Such a scheme combines the advantages of classical adaptive

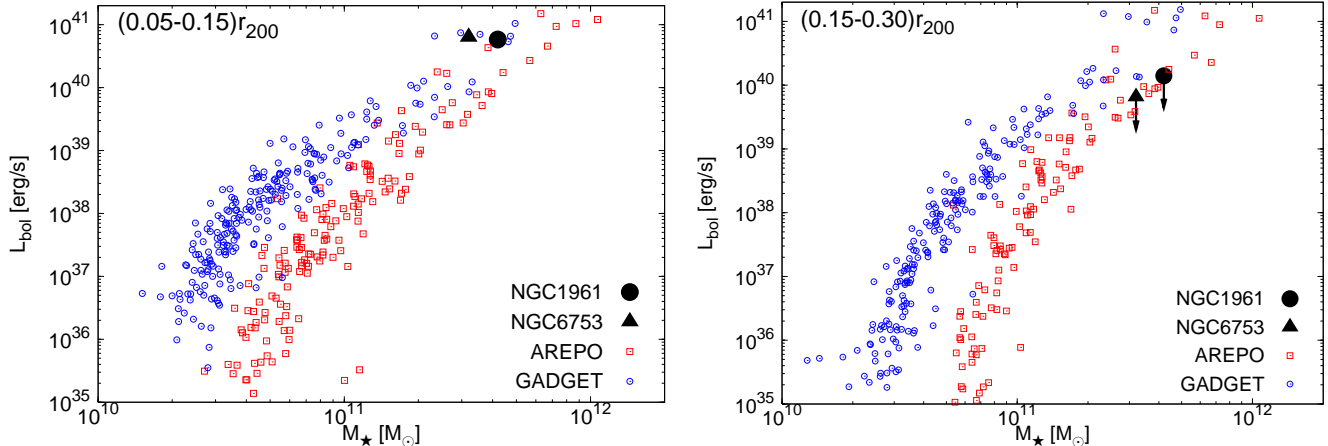


FIG. 8.— Predicted bolometric X-ray luminosities of the X-ray coronae around disk galaxies as a function of stellar mass for the $(0.05 - 0.15)r_{200}$ (left panel) and $(0.15 - 0.30)r_{200}$ radial cuts (right panel). Galaxies simulated by AREPO are shown with small boxes, whereas galaxies simulated by GADGET are marked with small circles. The observed X-ray luminosities and 3σ upper limits for NGC1961 and NGC6753 are shown with the big symbols. The statistical uncertainties on the observed X-ray luminosities are comparable with the size of the symbols.

mesh refinement (AMR) and SPH codes. For example, shocks, contact discontinuities, and mixing are significantly better resolved in AREPO than in classical SPH codes like GADGET.

The simulations discussed here adopt the cosmological parameters $\Omega_{m,0} = 0.27$, $\Omega_{\Lambda,0} = 0.73$, $\Omega_{b,0} = 0.045$, $\sigma_8 = 0.8$, $n_s = 0.95$ and $H_0 = 100 \text{ km s}^{-1} \text{ Mpc}^{-1} = 70 \text{ km s}^{-1} \text{ Mpc}^{-1}$. These parameters are consistent with the most recent WMAP-7 measurements (Komatsu et al. 2011). The simulation covers a volume of $(20 h^{-1} \text{ Mpc})^3$ sampled by 2×512^3 dark matter particles/cells with a mass of $3.722 \times 10^6 M_{\odot} h^{-1}$, the gravitational softening length is $1 h^{-1} \text{ kpc}$ comoving. The simulations contain also 512^3 SPH particles, and the AREPO (de-)refinement is setup such that the total number of Voronoi cells stays roughly constant also at 512^3 . This results in a SPH particle/cell mass of $7.444 \times 10^5 M_{\odot} h^{-1}$. Stars inherit their mass from SPH particles/cells, i.e. the mass of stellar particles is of the same order. For further details on the simulation setup we refer to Vogelsberger et al. (2012).

The GADGET and AREPO simulations follow the same physics. In particular, the simulations consist of a collisionless dark matter fluid and an ideal baryonic gas augmented with additional terms that account for radiative processes (optically-thin radiative cooling of a primordial mixture of helium and hydrogen plus a uniform, time-dependent ionising UV background) and star formation. Gas can collapse to high density and turn into stars. Both codes describe this process with the star formation and supernova feedback model introduced in Springel & Hernquist (2003) assuming a Salpeter IMF.

A comparison between the moving mesh code (AREPO) and the SPH code (GADGET) has been performed recently in a series of papers (Vogelsberger et al. 2012; Keres et al. 2012; Sijacki et al. 2012; Torrey et al. 2011; Bird et al. 2012). In their study, Vogelsberger et al. (2012) recognized a number of important differences between the two codes. Most importantly, significantly

more gas cools out of halos at low redshifts in AREPO than in GADGET, thereby yielding more massive and more extended stellar disks. This difference can be attributed to the stronger cooling flows that evolve in AREPO at low redshifts, yielding larger star-formation rates. At the same time, however, the hot X-ray coronae around massive galaxies are less dense, hence less luminous and have lower mass in AREPO than in GADGET. Additionally, the luminosity weighted gas temperatures are somewhat lower in AREPO than in GADGET. The hotter gas temperatures and the weaker gas cooling in the GADGET code can be explained by the different dissipative heating rates. Indeed, AREPO produces higher dissipative heating in the halo infall regions, and GADGET produces higher dissipation in the outer regions of halos. Vogelsberger et al. (2012) argue that the higher dissipation in GADGET is likely to be of spurious nature (see also Bauer & Springel 2012). Thus, the differences described above between the AREPO and GADGET simulations are purely due to the inaccuracies of the hydrodynamic solver.

Given the above differences between the AREPO and GADGET simulations, it is essential to observationally test these models. Confronting the observed and predicted properties of X-ray coronae around massive spiral galaxies is advantageous for the following two reasons. First, since the existence of hot gaseous coronae around massive disk galaxies is a basic prediction of galaxy formation models (White & Rees 1978), disk galaxies, such as NGC1961 and NGC6753, offer a clean observational test of these models. Second, the extended X-ray coronae are well-resolved in numerical simulations, hence their evolution can be followed through a large redshift range. Thus, in the following sections we compare the observed properties of hot gaseous coronae around NGC1961 and NGC6753 with those predicted by the AREPO and the GADGET simulations.

5.2. X-ray luminosities

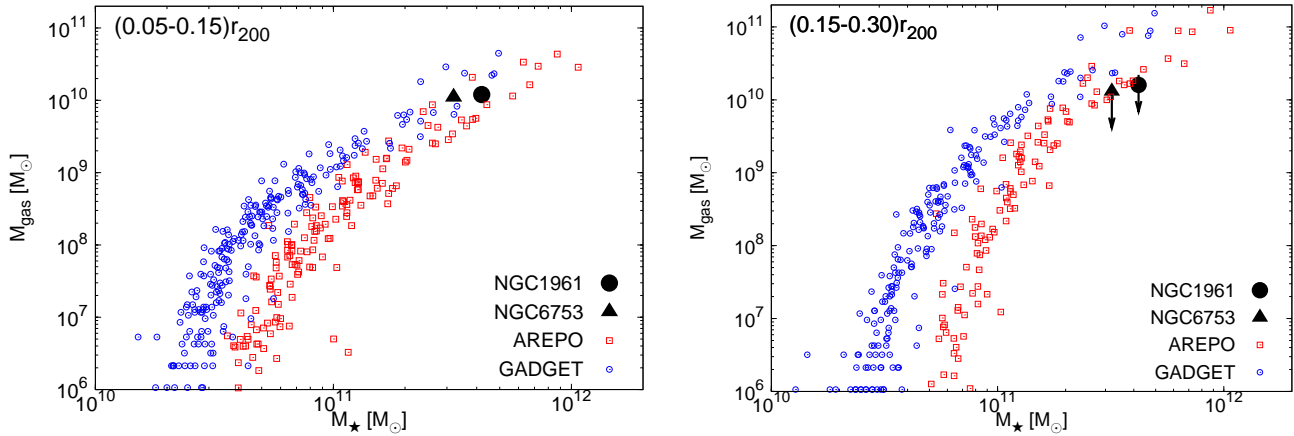


FIG. 9.— Predicted hot gas mass of the X-ray coronae around disk galaxies as a function of stellar mass for the $(0.05 - 0.15)r_{200}$ (left panel) and $(0.15 - 0.30)r_{200}$ regions (right panel). Only gas particles with temperature above 0.1 keV were used to compute the gas mass in the simulations. Galaxies simulated by the AREPO code are shown with small boxes, whereas galaxies simulated by the GADGET code are marked with small circles. The measured hot gas masses and 3σ upper limits for NGC1961 and NGC6753 are shown with the big symbols. The statistical uncertainties on the hot gas masses are comparable with the size of the symbols.

As a first probe, we confront the observed X-ray luminosities around NGC1961 and NGC6753 with those predicted by the AREPO and GADGET simulations. To facilitate the comparison with present-day and future simulations, all radial distances are converted to r_{200} units, where r_{200} is defined as the virial radius. The r_{200} radii of NGC1961 and NGC6753 are ~ 470 kpc and ~ 440 kpc, respectively (Section 2.2). Given the relatively small volume of the simulations, we did not make a specific selection of spiral galaxies. However, the studied volume mainly consists of spirals since the simulations do not include the physics required to form a significant population of ellipticals (for details see Section 5.6). We note that the simulated galaxies are not members of rich galaxy clusters.

For both NGC1961 and NGC6753, we compare the observed and predicted bolometric X-ray luminosities in two circular annuli with radii of $(0.05 - 0.15)r_{200}$ (inner region) and $(0.15 - 0.30)r_{200}$ (outer region). Note that the central regions ($< 0.05r_{200}$) are excluded due to the various contaminating factors associated with the stellar body of the galaxies (Section 1). In the $(0.05 - 0.15)r_{200}$ region, the X-ray luminosities are obtained from the best-fit spectra. In the $(0.15 - 0.30)r_{200}$ region, in the absence of X-ray gas detection, we place 3σ upper limits on the luminosities using adopted gas parameters (Section 4.3). The bolometric X-ray luminosities and upper limits for NGC1961 and NGC6753 are listed in Table 4.

In Figure 8 we show the predicted bolometric X-ray luminosities as a function of the stellar mass for the $(0.05 - 0.15)r_{200}$ and $(0.15 - 0.30)r_{200}$ regions. In these plots we mark the corresponding observed values and upper limits for NGC1961 and NGC6753. It is apparent from Figure 8 that, on average, the predicted X-ray coronae are more luminous in GADGET than in AREPO. Although this difference is clear in the inner region, it becomes even more evident in the outer regions. As a caveat, we note that above $\sim 2 \times 10^{11} M_{\odot}$ this difference is less evident, especially in the $(0.05 - 0.15)r_{200}$ radial range. In the inner region, the observed lumi-

TABLE 5
THE BEST-FIT PARAMETERS OF HOT GAS DENSITY PROFILES.

Galaxy	n_0 (cm^{-3})	r_c (kpc)	r_s^{\dagger} (kpc)	α	β	ϵ^{\dagger}	γ^{\dagger}
NGC1961	1.0×10^{-3}	18.1	400	4.40	0.29	0	3.0
NGC6753	1.0×10^{-3}	16.3	400	5.37	0.37	0	3.0

\dagger These parameters were fixed at the given value.

nosities for NGC1961 and NGC6753 fall closer to the GADGET predictions. However, given the relatively large scatter at the high mass end, no strong conclusions can be drawn. In the outer region, the 3σ upper limits are approximately consistent with the AREPO model predictions, but fall a factor of $\sim 2 - 10$ short of the GADGET predictions.

5.3. Hot gas mass and density profiles

In Figure 9 we present the predicted gas mass in the $(0.05 - 0.15)r_{200}$ and $(0.15 - 0.30)r_{200}$ regions as a function of the stellar mass. In both AREPO and GADGET simulations we only consider the hot gas components, whose temperature is above 0.1 keV. The observed gas masses and upper limits are given in Table 3.

Figure 9 demonstrates that GADGET predicts more massive X-ray coronae than AREPO. This difference is significantly larger in the outer region, thereby suggesting that the density profiles of the hot gas coronae fall more rapidly in the AREPO than in GADGET simulations. In the inner region, the observed gas mass is somewhat higher than that predicted by the moving mesh code but falls short of the SPH simulations. In the outer region, the 3σ upper limits on the gas mass are broadly consistent with the AREPO predictions. However, the GADGET simulation overpredicts the gas mass with at least factor of 2, but for most simulated galaxies with comparable stellar mass the predicted gas mass exceeds the 3σ upper limits with factors of about 8 – 10.

To further probe the structure formation models, we compare the observed and predicted electron density pro-

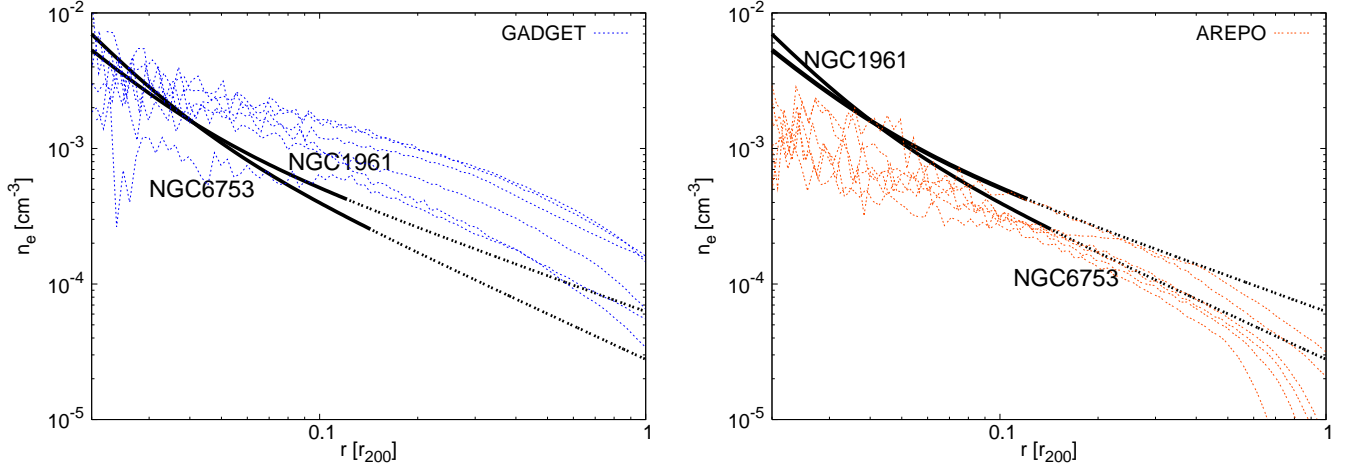


FIG. 10.— Observed and predicted electron density profiles as the function of the radius for the GADGET (left panel) and AREPO (right panel) simulations. Note that the radius is measured in units of r_{200} . The thick solid lines show the observed density profiles, whereas the short dashed thick lines show the extrapolated density profiles based on the best-fit β -models (Section 5.3). The statistical uncertainties on the observed profiles are comparable with the difference between the two profiles. The predicted density profiles originate from six representative simulated galaxies, whose stellar masses are comparable with those of NGC1961 and NGC6753.

files, which allow a more detailed comparison between the observed and simulated gas distributions. Hence not only the volume averaged quantities can be confronted but also the normalization and the shape of the density profiles will be tested. Since the hot gas is only detected to $\sim 0.15r_{200}$, we extrapolate our measurements out to the virial radius. To this end, we describe the observed surface brightness distribution in the $(0.02 - 0.15)r_{200}$ region with a modified β -model. Under the assumption of constant metallicity gas, we derive the emission measure profile at a projected radius (r) following Vikhlinin et al. (2006):

$$n_p n_e = n_0^2 \frac{(r/r_c)^{-\alpha}}{(1 + r^2/r_c^2)^{3\beta - \alpha/2}} \frac{1}{(1 + r\gamma/r_s^\gamma)^{\epsilon/\gamma}}. \quad (6)$$

This β -model consists of a power law-type cusp and also describes the possible steepening of X-ray surface brightness profiles at large radii (Vikhlinin et al. 2006). The obtained best-fit parameters of the emission measure profile are listed in Table 5. To compare the observed electron density profiles with those produced by AREPO and GADGET, we extract the density profiles of six representative galaxies with stellar masses in the range of $(2.5 - 4.9) \times 10^{11} M_\odot$, which is comparable with those of NGC1961 and NGC6753. We stress that the simulated electron density profiles do not correspond to the same halos, hence the simulated GADGET and AREPO profiles are not directly comparable. This is due to the fact that, while both simulations are affected by the so-called overcooling problem, the stellar mass of galaxies in the AREPO simulations is larger than that in the GADGET simulations (see Section 5.6 for details). Moreover, given that the virial radii of the simulated galaxies are somewhat different than that of NGC1961 and NGC6753, the density profiles in Figure 10 cannot be directly compared with Figure 9, which shows the integrated gas mass as a function of stellar mass. The selected simulated galaxies have a SFR of $10 - 20 M_\odot \text{ yr}^{-1}$ at $z = 0$ in the AREPO simulation (in the GADGET it is about a factor of two lower), which is also comparable with the observed val-

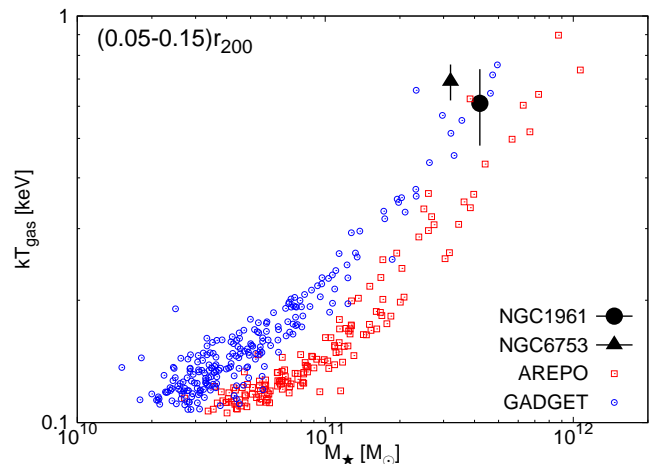


FIG. 11.— Predicted hot gas temperatures of the X-ray coronae as a function of the stellar mass for the $(0.05 - 0.15)r_{200}$ range. Simulated galaxies are shown with the small boxes (AREPO) and small circles (GADGET). The observed hot gas temperatures for NGC1961 and NGC6753, obtained from the best-fit spectra, are shown with the big filled symbols.

ues for NGC1961 and NGC6753. As a caveat, we mention that the limited numerical resolution of the simulations implies that halos are not well resolved close to the gravitational softening scale. Therefore, the inner regions ($\lesssim 0.05r_{200}$) close to that scale are not sampled by a large number of particles, which causes the more noisy profiles towards the inner parts of the halos.

The comparison between observed and simulated electron density profiles are depicted in Figure 10. Although the density profiles predicted by GADGET show a large scatter, their overall distribution strikingly differs from the observed ones at all radii (left panel of Figure 10). Indeed, the simulated GADGET density profiles are significantly flatter than those observed (and extrapolated) for NGC1961 and NGC6753, and most of them predict too high densities in the $(0.05 - 1)r_{200}$ radial range. Although

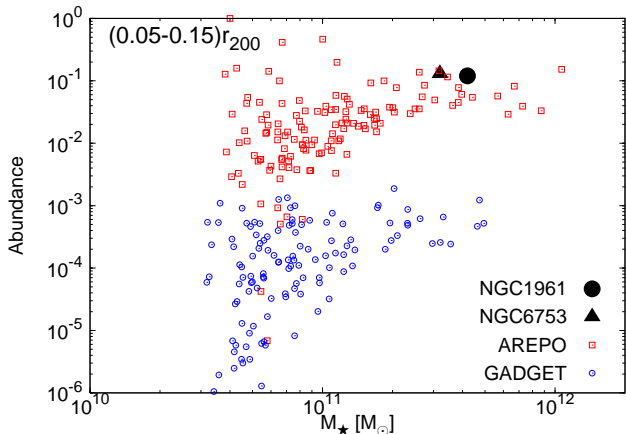


FIG. 12.— Predicted abundances of the X-ray coronae vs stellar mass for the $(0.05 - 0.15)r_{200}$ range. Galaxies simulated by AREPO are shown with boxes, and galaxies simulated by GADGET are marked with circles. The observed abundances for NGC1961 and NGC6753 are shown with the big symbols. The statistical uncertainties on the measured values are comparable with the size of the symbols.

in the innermost regions ($< 0.05r_{200}$) the predicted and observed electron densities agree with each other, this result is not conclusive since the innermost regions of galaxies cannot be used to probe galaxy formation models. At larger radii ($> 0.5r_{200}$) the simulated profiles fall much faster than the extrapolated ones, which, at least partly, may be explained by the absence of efficient supernova and AGN feedback in the model.

The density profiles predicted by the AREPO simulations also exhibit a notable scatter (right panel of Figure 10). Although the predicted densities fall short of the observed values in the innermost regions, the shape of the density profiles and the observed and predicted n_e values are broadly consistent in the $(0.05 - 0.5)r_{200}$ range. We mention that within $\sim 0.05r_{200}$ the X-ray emission is dominated by gas produced in the course of the stellar evolution of the galaxies, therefore this region does not test the extended X-ray coronae. Beyond $\sim 0.5r_{200}$ the density drops sharper than the extrapolated profiles of NGC1961 and NGC6753. The truncated density profile in the simulation is most likely due to the absence of efficient supernova and AGN feedback in the models. Implementing efficient energy feedback will likely result in more extended gas distributions, resulting in a better agreement with the observed profiles at large galactocentric radii.

Based on the density profiles we conclude that (1) AREPO describes the observed density profiles better than GADGET at radii $< 0.5r_{200}$; and (2) at larger radii both simulations fail to reproduce the shape of the extrapolated profiles, presumably due to the absence of efficient feedback in the models.

5.4. Hot gas temperature

In Figure 11 we depict the predicted hot gas temperatures in the $(0.05 - 0.15)r_{200}$ radial range as the function of the stellar mass. The predicted temperatures are luminosity-weighted values.

In general, GADGET predicts higher gas temperatures

than AREPO throughout the entire stellar mass range. For both simulations, the expected temperatures are in the relatively narrow $kT = 0.3 - 0.7$ keV range for galaxies with $\sim 4 \times 10^{11} M_{\odot}$. For NGC1961 and NGC6753 the observed gas temperatures are $kT \sim 0.6 - 0.7$ keV, which places them at the high end of the predictions. The observed values are in fair agreement with the SPH simulation and exceed the values predicted by the moving mesh code.

However, at present, neither simulation code implements efficient energy feedback from supernovae and supermassive black holes, which serves as an additional heating source. Therefore, including the efficient feedback in the simulations will yield higher gas temperatures, and possibly better agreement with the observed values. We note that based on the presently available X-ray data, the temperature distribution of the hot gas cannot be studied in detail. To better explore the temperature structure of X-ray coronae, further deep observations are required.

5.5. Abundances of the hot gas

As a final test, we investigate the observed and predicted abundances of the hot X-ray coronae in the $(0.05 - 0.15)r_{200}$ radial cut. The observed abundances for NGC1961 and NGC6753 are the best-fit values from the spectral fitting procedure, which are given in Table 3. The predicted values are luminosity-weighted abundances.

In Figure 12 we show the predicted abundances for the AREPO and GADGET simulations as a function of stellar mass. The observed values for NGC1961 and NGC6753 are overplotted. For the two structure formation simulations, there is a striking difference between the predicted abundances. Whereas for galaxies with a few $\times 10^{11} M_{\odot}$ stellar mass, AREPO predicts ~ 0.1 Solar abundance. The expected values in GADGET are about two orders of magnitude less, $\sim 10^{-3}$ Solar. The observed values for NGC1961 and NGC6753 are ~ 0.1 Solar, which are in good agreement with that predicted by AREPO. We thus conclude that the observed abundances of the hot gas around NGC1961 and NGC6753 strongly favor the moving mesh code over the SPH simulations.

The abundance difference between the codes is caused by two effects. First, due to the increased cooling, AREPO exhibits higher star formation rates than GADGET, which is attributed to the different dissipative heating rates (Section 5.1). Since metal production in the simulations is tied to star formation assuming a fixed yield, the higher star formation in AREPO automatically leads to a production of higher abundances. Second, the mixing is more efficient in AREPO than in GADGET. This point is related to the intrinsic mixing problems of standard SPH codes. In the GADGET simulations, metals are transported by individual SPH particles and they do not undergo any explicit metal diffusion process. Contrarily, the metals are advected and can mix well within the gas in the AREPO code. Accordingly, metals stay closer to the central part of galaxies and haloes in GADGET compared to AREPO. This difference becomes particularly apparent for more massive galaxies, where enrichment of halos through mixing is highly ineffective in GADGET (Figure 12). In massive galaxies the abundances differ by about two orders of magnitude between the two simulations, but this dif-

ference gets progressively lower in smaller mass systems. The mixing of metals in the AREPO code will be further discussed in the upcoming work by Vogelsberger et al. (2013, in preparation). Finally, we note that the inclusion of explicit supernova winds is another source of halo gas enrichment, which is not included in our simulations.

5.6. Limitations of the present simulations

Although AGN feedback and galactic winds are believed to have a profound impact on the evolution of galaxies, the galaxy formation simulations discussed in this paper do not incorporate efficient energy feedback from AGN and supernovae. The impact of AGN feedback is observed in different scales in the local Universe: in galaxies (e.g. Finoguenov et al. 2001; Jones et al. 2002; Kraft et al. 2011), galaxy groups (e.g. David et al. 2009; Gitti et al. 2010; Randall et al. 2011), and galaxy clusters (e.g. Fabian et al. 2000; Forman et al. 2005; Nulsen et al. 2005; Bogdán et al. 2011a). Moreover, theoretical studies also point out that the AGN feedback is capable of heating the cool gas and expelling it to larger radii, thereby quenching the star-formation and regulating the growth of supermassive black holes (Silk & Rees 1998; Di Matteo et al. 2005; Sijacki et al. 2007). Galactic winds driven by the energy input of supernovae eject metal-rich gas to large radii, thereby enriching the extraplanar gas (Oppenheimer & Davé 2006). Additionally, galactic winds play a major role in reproducing the cosmic star-formation history at high redshifts (Schaye et al. 2010). Furthermore, implementing efficient AGN and supernova feedback will address one of the major shortcomings of the present models: the so-called overcooling of galaxies. Without efficient feedback too much gas cools out of the halos both in the AREPO and the GADGET simulations, hence produce overly massive stellar components relative to their dark matter halos. Although both simulation codes are affected by the overcooling problem, galaxies in AREPO are more massive

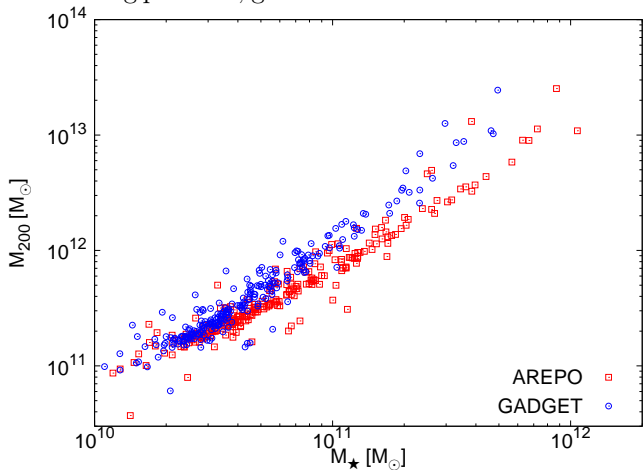


FIG. 13.— Virial mass as a function of stellar mass for the AREPO and GADGET simulations. Galaxies simulated by the AREPO code are shown with boxes, whereas galaxies simulated by the GADGET code are marked with circles. Note that both simulations suffer from the so-called overcooling problem, that is too much gas cools out of the halos, thereby producing too massive stellar disks relative to their dark matter halos. The stellar masses of NGC1961 and NGC6753 are $4.2 \times 10^{11} M_{\odot}$ and $3.2 \times 10^{11} M_{\odot}$, respectively.

than their counterparts in GADGET (Figure 13).

The present models also do not incorporate the contribution of metal cooling to the emission. However, the cooling of metal species plays a significant role at the observed sub-keV temperatures (van de Voort et al. 2011). Indeed, metal cooling notably influences the temperature structure, hence the X-ray luminosity of the hot gas. Metal line cooling also increases the star formation rates, and affects the build-up of galaxies. On the other hand, AGN and supernova feedback typically heat the gas and decrease the star formation rates, such that missing feedback and missing metal line cooling partially cancel each other.

In subsequent papers we will investigate structure formation simulations, which incorporate the above discussed missing physics. Thus, the forthcoming studies will lead to a physically more realistic comparisons between the observed X-ray coronae and numerical models.

5.7. Synopsis about the AREPO and GADGET simulations

In this section we compared the observed physical properties of hot X-ray coronae around two massive spiral galaxies with those predicted by two structure formation simulations. The moving mesh code (AREPO) and the SPH based code (GADGET) uses fully identical sub-resolution physics and gravity solver, but they employ different methods to solve the equations of hydrodynamics. Based on the comparison we reached the following major conclusions:

1. In the $(0.05 - 0.15)r_{200}$ radial range the X-ray luminosities and hot gas masses broadly agree with both simulations. However, in the $(0.15 - 0.30)r_{200}$ region the upper limits for X-ray luminosities and gas masses are more consistent with AREPO, since GADGET overpredicts both quantities.
2. The observed (and extrapolated) density profiles in the $(0.05 - 0.5)r_{200}$ radial range are in fair agreement with those predicted by AREPO. Contrarily, GADGET predicts markedly different density profiles, which disagree with the shape and normalization of the observed and extrapolated profiles in the $(0.05 - 1)r_{200}$ region.
3. The observed abundances in the $(0.05 - 0.15)r_{200}$ region are in good agreement with those predicted by AREPO, but exceed the predictions of GADGET by about two orders of magnitude.

Although the above listed points suggest that the moving mesh code gives a significantly better description of structure formation, further observational and theoretical efforts are required before definite conclusions can be drawn. On the observational side, it is necessary to further push the limits of X-ray observations, and probe the X-ray coronae at even larger radii. Such observations would allow the more precise comparison of observations and numerical models. Moreover, the parameter space needs to be better explored, that is the X-ray coronae of other, preferably lower mass, galaxies should be observed and characterized. On the theoretical side, efficient energy feedback from AGN and supernovae must be included along with cooling from metal species. The comparison with physically more realistic models will lead

to a significantly better understanding of the physical processes, which influence galaxy formation models.

6. DISCUSSION

6.1. *The role of starburst driven winds*

Although the goal of the present work is to explore the hot gaseous X-ray coronae around massive spiral galaxies, it is feasible that a certain fraction of the detected hot gas was uplifted from the galactic disks. In principle, galaxies with sufficiently high specific star-formation rates are capable of driving starburst driven winds. Based on theoretical computations, Strickland et al. (2004b) estimated that supernova blowout occurs at the (surface area) specific SN rate $\gtrsim 25 \text{ SN Myr}^{-1} \text{ kpc}^{-2}$, where the surface area is derived as the square of the D_{25} diameter. In fair agreement with the theoretical computations, Strickland et al. (2004b) detect extraplanar X-ray emission in galaxies, whose specific SN rates are $\gtrsim 40 \text{ SN Myr}^{-1} \text{ kpc}^{-2}$.

To probe the importance of SN driven winds in NGC1961 and NGC6753, we compute their area specific SN rates. Following Heckman et al. (1990), the SN rate is derived from $R_{\text{SN}} = 0.2 L_{\text{FIR}} / 10^{11} L_{\odot}$, where L_{FIR} is the total far-infrared luminosity. For NGC1961 and NGC6753 we observe $L_{\text{FIR,NGC1961}} = 9.0 \times 10^{10} L_{\odot}$ and $L_{\text{FIR,NGC6753}} = 6.8 \times 10^{10} L_{\odot}$ (Section 3.3), which correspond to the SN rates of $R_{\text{SN,NGC1961}} = 0.18 \text{ yr}^{-1}$ and $R_{\text{SN,NGC6753}} = 0.14 \text{ yr}^{-1}$, respectively. Based on these values and the D_{25} major axis diameters, we estimate area specific SN rates of $\sim 36 \text{ Myr}^{-1} \text{ kpc}^{-2}$ for NGC1961 and $\sim 97 \text{ Myr}^{-1} \text{ kpc}^{-2}$ for NGC6753. The value obtained for NGC1961 is comparable albeit somewhat lower than the observational lower limit required for SN blowout. In NGC6753 the specific SN rate is higher than the critical rate for SN blowout, suggesting that a fraction of the detected warm gas may be uplifted from the disk.

Despite the relatively high specific SN rates, the following four arguments suggest that the detected X-ray coronae around NGC1961 and NGC6753 cannot be entirely attributed to starburst driven winds. 1) The morphology of the X-ray gas (Figures 3, 4, 6) is fairly symmetric. This indicates that the hot gas resides in hydrostatic equilibrium in the potential well of the galaxies, and is not in a bipolar starburst driven outflow. 2) Although the specific SN rates are comparable or exceed the criteria for SN blowout, the derived values are significantly lower than that observed in starburst galaxies, for example in M82 ($\sim 1200 M_{\odot} \text{ Myr}^{-1} \text{ kpc}^{-2}$) or NGC253 ($\sim 180 M_{\odot} \text{ Myr}^{-1} \text{ kpc}^{-2}$) (Strickland et al. 2004b). 3) The extraplanar X-ray emission in starburst galaxies is confined to within $\sim 15 \text{ kpc}$ (Strickland et al. 2004a), whereas we detect hot gas out to $\sim 60 \text{ kpc}$ around NGC1961 and NGC6753. Additionally, we emphasize that the central $0.05 r_{200}$ ($\sim 23 \text{ kpc}$) regions are excluded when studying the properties of the diffuse X-ray emission. 4) The cooling time of the hot gas is on the time scale of $\sim 50 \text{ Gyrs}$ in the inner region. Therefore, the hot gas can be treated as quasi-static gas as opposed to a starburst driven wind. Taken together, this evidence suggests that only fraction of the warm gas around NGC1961 and NGC6753 could originate from starburst driven winds.

The above considerations demonstrate that *at the*

present epoch the X-ray appearance of NGC1961 and NGC6753 is not determined by starburst driven winds. However, at higher redshifts gas-rich galaxy mergers occurred more frequently, which could have triggered more active phases, possibly leading to starburst driven winds. Such winds do not only expel a notable amount of gas to larger radii, but also play a major role in enriching the hot extraplanar gas, which is reflected by the non-zero abundance of the hot gas around NGC1961 and NGC6753. Thus, at some point of their evolution, the hot X-ray coronae are likely to be influenced by starburst driven winds.

6.2. *Baryon mass fraction*

The detection of hot X-ray coronae around NGC1961 and NGC6753 allows us to estimate their baryon budget and derive their baryon mass fraction. To account for the baryon content, we consider the total hot X-ray gas mass, the stellar mass of the galaxies, the cold gas mass, and the stellar mass of the group member galaxies. The detailed mass budget is given in Table 6.

In massive galaxies, such as NGC1961 and NGC6753, the hot X-ray emitting gas adds a notable contribution to the baryon budget. Therefore, we derive the confined hot gas mass by extrapolating the density profiles out to the virial radius (Section 5.3). For NGC1961 and NGC6753 the obtained total hot gas masses within r_{200} are $9.4 \times 10^{11} M_{\odot}$ for NGC1961 and $3.9 \times 10^{11} M_{\odot}$, respectively. We emphasize that these numbers should only be considered as a crude estimate due to the following systematic and statistical uncertainties: 1) The major source of uncertainty originates from the unexplored nature of the hot gas beyond $0.15 r_{200}$ radius. Indeed, a temperature and/or abundance gradient could drastically alter the extrapolated density profiles, and hence the total gas mass within the virial radius. 2) The hot gas may not have a spherically symmetric distribution at large radii. 3) The applied r_{200} radii may deviate from the real r_{200} radii. 4) Statistical uncertainties in the best-fit parameters of the β -model. 5) Systematic uncertainties in the derived mass-to-light ratios.

The stellar mass is derived from the 2MASS K-band images and the K-band mass-to-light ratios (Section 3.2). For the cold gas mass we use the HI mass of $4.7 \times 10^{10} M_{\odot}$ for NGC1961 (Haan et al. 2008), and we estimate the HI mass of about $2 \times 10^{10} M_{\odot}$ for NGC6753 (Haynes & Giovanelli 1984). Since both galaxies are located in poor groups (Fouque et al. 1992), the baryon mass of these galaxies should also be included in the baryon budget. The baryon mass of the group members is dominated by their stellar mass, which we estimate based on their K-band luminosity, using $M_{\star}/L_K = 0.8$, and assuming that they lie at the same distance as NGC1961 and NGC6753. Finally, we mention that within the *XMM-Newton* FOV we do not detect hot intragroup medium around the sample galaxies. For NGC1961 this conclusion is confirmed by the archival *Chandra* observations (Anderson et al. 2011).

The total baryonic masses of NGC1961 and NGC6753 are $M_{\text{b,tot}} = 1.55 \times 10^{12} M_{\odot}$ and $M_{\text{b,tot}} = 1.00 \times 10^{12} M_{\odot}$, respectively (Table 6). The estimated dark matter halo mass of the galaxies are $M_{\text{DM}} = 1.2 \times 10^{13} M_{\odot}$ and $M_{\text{DM}} = 1.0 \times 10^{13} M_{\odot}$, respectively (Section 2.2). Defin-

TABLE 6
MASS BUDGET OF NGC1961 AND NGC6753.

Galaxy	M_* (M_\odot)	$M_{\text{gas,hot}}$ (M_\odot)	$M_{\text{gas,cold}}$ (M_\odot)	M_{group} (M_\odot)	$M_{\text{b,tot}}$ (M_\odot)	M_{DM} (M_\odot)	f_b
	(1)	(2)	(3)	(4)	(5)	(6)	(7)
NGC1961	4.2×10^{11}	9.4×10^{11}	4.7×10^{10}	1.4×10^{11}	1.55×10^{12}	1.2×10^{13}	0.11
NGC6753	3.2×10^{11}	3.9×10^{11}	2.0×10^{10}	2.7×10^{11}	1.00×10^{12}	1.0×10^{13}	0.09

Note. Columns are as follows. (1) Total stellar mass of the sample galaxies. (2) Estimated hot X-ray gas mass within the virial radius, obtained from the extrapolation of the β -models (Section 6.2). (3) Cold gas mass. (4) Total stellar mass of group members. (5) Total baryon mass, which is the sum of columns (1) – (4). (6) Estimated mass of the dark matter halo. (7) Baryon mass fraction, defined as $f_b = M_{\text{b,tot}}/(M_{\text{DM}} + M_{\text{b,tot}})$.

ing the baryon mass fraction as $f_b = M_{\text{b,tot}}/(M_{\text{DM}} + M_{\text{b,tot}})$, we obtain $f_b \approx 0.11$ for NGC1961 and $f_b \approx 0.09$ for NGC6753.

The cosmic baryon mass fraction has been precisely measured by the *Wilkinson Microwave Anisotropy Probe* (WMAP), yielding $f_{\text{b,WMAP}} = 0.171 \pm 0.009$ (Dunkley et al. 2009). This value is significantly larger than that observed in NGC1961 and NGC6753, implying that $\sim 30 - 50\%$ of the baryons are missing. This result is in agreement with observations of other disk galaxies, and galaxy groups (see Bregman 2007, for a review). We note that a factor of ~ 2 lower M_{DM} would imply a baryon mass fraction that is in agreement with the cosmic value. However, the quoted dark matter mass is broadly consistent with values found for massive spiral galaxies (Mandelbaum et al. 2006). Hence the missing baryon problem appears to be genuine. As a further caveat, we emphasize again the large uncertainties associated with the determination of the hot gas mass within the virial radius. This plays a particularly important role given that $\sim 50\%$ of the total baryon mass is in the form of hot gas in the (yet undetected) outer parts of the halo. In principle, the real gas density profile beyond $\sim 0.15r_{200}$ may significantly deviate from the extrapolated ones, yielding a very different total hot gas mass. For example, if the hot gas mass of NGC1961 and NGC6753 is 2 – 3 times more than that estimated based on the density profiles, the resulting f_b would be approximately consistent with the cosmic baryon mass fraction. To clearly determine the baryon budget of these (and other) spiral galaxies, further deep X-ray observations are required, which probe their hot gas content to larger radii.

6.3. Iron bias and abundances

The major parameters of the X-ray coronae, listed in Tables 3 and 4, are deduced from the best-fit spectra. However, two well-known complications are associated with the analysis of thermal X-ray spectra. One of them is the iron bias (e.g. Buote et al. 2000; Bogdán et al. 2012), and the other is the degeneracy between the emission measure and the abundance of the thermal component (e.g. David et al. 2006).

In principle, the observed metal abundances may partly be influenced by the iron-bias, which appears if either a multi-temperature plasma or a temperature gradient is fit with a single temperature model. If the hot gas around NGC1961 and NGC6753 has a complex thermal structure, the measured metal abundances may be underestimated. The degeneracy between the emission mea-

sure and the abundances of the thermal model may have an impact on the observed gas parameters. For example, if the abundance of the X-ray gas is not strictly sub-solar, but is about Solar, i.e. ~ 10 times higher than measured, the gas densities, gas masses, and cooling times must be reduced by a factor of ~ 3.3 .

To address these points, the thermal and abundance structure of the hot gas must be better explored. However, based on the presently available *XMM-Newton* data set, the application of more complex (e.g. multi-temperature) models is not feasible. Therefore, additional deep X-ray observations of NGC1961 and NGC6753 are needed to settle this issue.

6.4. Future prospects

To further probe the luminous X-ray coronae and constrain structure formation models, it is essential to identify X-ray coronae around other massive spiral galaxies. The large effective area of *XMM-Newton* makes it especially suitable for the detection of hot gaseous coronae. Indeed, by combining the data of the three EPIC cameras, it is possible to collect a fairly large number of photons in moderately deep observations. Moreover, the large FOV allows one to explore the coronae out to sufficiently large radii. A disadvantage of *XMM-Newton* is its relatively high instrumental background level, which results in notable systematic uncertainties, thereby hindering the study of faint X-ray emission. For example, in NGC1961 and NGC6753 the systematic uncertainties dominate beyond ~ 60 kpc radius, hence our understanding of their X-ray coronae would not significantly improve at larger radii even with much deeper observations. *Chandra* has a lower level of instrumental background, making it ideal to explore the coronae at large galactocentric distances. However, due to the smaller effective area of *Chandra* it takes significantly longer to collect a meaningful number of photons.

The upcoming *eROSITA* mission will perform a four year all sky-survey program (Predehl et al. 2010), during which a mean exposure time of 2.0 ks will be observed. This mission will play a major role in identifying the X-ray coronae of all nearby massive spiral galaxies. However, due to the relatively short exposure time of the *eROSITA* survey, follow-up observations will be required to characterize the X-ray coronae, which can be done with *Chandra*, *XMM-Newton*, or *eROSITA* itself.

On a longer time scale, the *Square Meter Arcsecond Resolution X-ray Telescope (SMART-X)* mission will offer an outstanding possibility to characterize hot X-ray coronae around massive spiral galaxies (Vikhlinin et al.

2012). With its large FOV ($22' \times 22'$) and large effective area (2.3 m^2 at 1 keV) the *SMART-X* Active Pixel Sensor Imager will collect 5500 counts around NGC1961 in a 10 ks observation in the 0.7 – 2 keV energy range from the region between 25 – 45 kpc. This will drastically increase the signal-to-noise ratio, thereby allowing the study of X-ray coronae in unprecedented details. Additionally, with the use of the X-ray Microcalorimeter Imaging Spectrometer aboard *SMART-X* the outer regions of the X-ray coronae can also be explored. Indeed, with the microcalorimeter the soft Galactic emission can be differentiated from the hot X-ray gas corona. Thus, it will be feasible to investigate the X-ray coronae of a large sample of disk galaxies, thereby further constraining galaxy formation scenarios.

7. CONCLUSIONS

In this paper, we study the hot gaseous X-ray coronae around two “normal” spiral galaxies, NGC1961 and NGC6753, based on moderately deep *XMM-Newton* observations. Since luminous X-ray coronae are a fundamental prediction of structure formation models, we use our observations to probe hydrodynamical structure formation simulations. Our results are:

1. We detect luminous X-ray coronae around NGC1961 (in good agreement with Anderson et al. 2011) and NGC6753. In both galaxies, the hot gas extends to ~ 60 kpc, which significantly exceeds their optical radii. The spatial distribution of the hot gas is fairly round and symmetric, indicating that the X-ray gas resides in hydrostatic equilibrium in the potential well of the galaxies.
2. We find that the observed characteristics of the coronae in NGC6753 are fairly similar to NGC1961. In particular, within the $(0.05 - 0.15)r_{200}$ region we measure gas temperatures of $kT \sim 0.6$ keV and abundances of ~ 0.12 Solar. The cooling time scale of the gas is ~ 50 Gyrs, implying its quasi-static nature. The bolometric X-ray luminosity of the hot gas within the same region is $\sim 6 \times 10^{40} \text{ erg s}^{-1}$ for both galaxies.
3. We derive the baryon mass fraction of NGC1961 and NGC6753, and obtain $f_b \approx 0.11$ and $f_b \approx$

0.09, respectively. These values are lower than the cosmic baryon mass fraction, indicating that $\sim 30 - 50\%$ of the baryons are missing from these galaxies. However, large uncertainties are associated with the derivation of the total hot gas mass within the virial radius, which could bias the obtained values of f_b .

4. The observed characteristics of the X-ray coronae are compared with the moving mesh code AREPO and the SPH-based code GADGET. The implemented subresolution physics and the gravity solver are identical in the two codes, but they use different methods to solve the equations of hydrodynamics. We find that, while neither model gives a perfect description, the AREPO code better reproduces the luminosities, gas masses, and abundances observed around NGC1961 and NGC6753. Additionally, the shape of the observed density profiles are also in better agreement with the moving mesh code within $\sim 0.5r_{200}$. However, neither model incorporates efficient feedback from AGN and supernovae, which could significantly alter the simulated properties of the coronae.

Acknowledgements. We thank the anonymous referee for useful comments. We thank Alexey Vikhlinin for helpful discussions about *SMART-X*, Volker Springel for careful reading, and Rob Crain for critical comments. This work uses observations obtained with *XMM-Newton*, an ESA science mission with instruments and contributions directly funded by ESA Member States and NASA. This publication makes use of data products from the Two Micron All Sky Survey, which is a joint project of the University of Massachusetts and the Infrared Processing and Analysis Center/California Institute of Technology, funded by the National Aeronautics and Space Administration and the National Science Foundation. In this work the NASA/IPAC Extragalactic Database (NED) have been used. The authors acknowledge use of the HyperLeda database (<http://leda.univ-lyon1.fr>). ÁB acknowledges support provided by NASA through Einstein Postdoctoral Fellowship grant number PF1-120081 awarded by the Chandra X-ray Center, which is operated by the Smithsonian Astrophysical Observatory for NASA under contract NAS8-03060. WF and CJ acknowledge support from the Smithsonian Institution.

REFERENCES

- Anderson, M. E. & Bregman, J. N., 2011, *ApJ*, 737, 22
 Barnes, J. & Hut, P., 1986, *Nature*, 324, 446
 Bauer, A. & Springel, V., 2012, *MNRAS*, 423, 2558
 Bell, E. F., McIntosh, D. H., Katz, N. & Weinberg, M. D., 2003, *ApJS*, 149, 289
 Benson, A. J., Bower, R. G., Frenk, C. S. & White, S. D. M., 2000, *MNRAS*, 314, 557
 Bertin, E. & Arnouts, S., 1996, *A&AS*, 117, 393
 Bird, S., Vogelsberger, M., Sijacki, et al., 2012, [arXiv:1209.2118](https://arxiv.org/abs/1209.2118)
 Bogdán, Á., Gilfanov, M., 2008, *MNRAS*, 388, 56
 Bogdán, Ákos, Kraft, R. P., Forman, W. R., et al., 2011a, *ApJ*, 743, 59
 Bogdán, Á., Gilfanov, M., 2011b, *MNRAS*, 418, 1901
 Bogdán, Á., David, L. P., Jones, C., Forman, W. R. & Kraft, R. P., 2012, *ApJ*, 758, 65
 Bogdán, Á., Forman, W. R., Kraft, R. P., & Jones, C., *ApJ*, in press, [arXiv:1306.0643](https://arxiv.org/abs/1306.0643)
 Bourdin, H. & Mazzotta, P., 2008, *A&A*, 479, 307
 Bourdin, H., Mazzotta, P., Markevitch, M., Giacintucci, S. & Brunetti, G., 2013, *ApJ*, 764, 82
 Bregman, J. N., 2007, *ARA&A*, 45, 221
 Buote, D. A., 2000, *MNRAS*, 311, 176
 Calzetti, D., Armus, L., Bohlin, R. C., et al., 2000, *ApJ*, 533, 682
 Carter, J. A. & Read, A. M., 2007, *A&A*, 464, 1155
 Combes, F., Baker, A. J., Schinnerer, E., et al., 2009, *A&A*, 503, 73
 Crain, R. A., McCarthy, I. G., Frenk, C. S., Theuns, T. & Schaye, J., 2010, *MNRAS*, 407, 1403
 Dai, X., Anderson, M. E., Bregman, J. N. & Miller, J. M., 2012, *ApJ*, 755, 107
 David, L. P., Jones, C., Forman, W., Vargas, I. M. & Nulsen, P., 2006, *ApJ*, 653, 207
 David, L. P., Jones, C., Forman, W., et al., 2009, *ApJ*, 705, 624
 de Vaucouleurs, G., et al., *Third Reference Catalogue of Bright Galaxies*. Springer-Verlag. (1991)
 Dickey, J. M., Lockman, F. J., 1990, *ARA&A*, 28, 215

- Di Matteo, T., Springel, V. & Hernquist, L., 2005, *Nature*, 433, 604
- Dunkley, J., Komatsu, E., Nolita, M. R., 2009, *ApJS*, 180, 306
- Fabian, A. C., Sanders, J. S., Ettori, S., et al., 2000, *MNRAS*, 318, L65
- Finoguenov, A. & Jones, C., 2001, *ApJ*, 547, L107
- Forman, W., Jones, C. & Tucker, W., 1985, *ApJ*, 293, 102
- Forman, W., Nulsen, P., Heinz, S., et al., 2005, *ApJ*, 635, 894
- Fouque, P., Gourgoulhon, E., Chamaraux, P. & Paturel, G., 1992, *A&AS*, 93, 211
- Gilfanov, M., 2004, *MNRAS*, 349, 146
- Gitti, M., O'Sullivan, E., Giacintucci, S., et al., 2010, *ApJ*, 714, 758
- Grevesse, N. & Sauval, A. J., 1998, *SSRv*, 85, 161
- Grimm, H.-J., Gilfanov, M. & Sunyaev, R., 2003, *MNRAS*, 339, 793
- Haan, S., Schinnerer, E., Mundell, C. G., García-Burillo, S. & Combes, F., 2008, *AJ*, 135, 232
- Haynes, M. P. & Giovanelli, R., 1984, *AJ*, 89, 758
- Heckman, T. M., Armus, L. & Miley, G. K., 1990, *ApJS*, 74, 833
- Helou, G., Khan, I. R., Malek, L. & Boehmer, L., 1988, *ApJS*, 68, 151
- Hernquist, L., 1987, *ApJS*, 64, 715
- Hockney, R. W. & Eastwood, J. W., 1981, *Computer Simulation Using Particles*, New York
- Jarrett, T. H., Chester, T., Cutri, R., Schneider, S. E. & Huchra, J. P., 2003, *AJ*, 125, 525
- Jones, C., Forman, W., Vikhlinin, A., et al., 2002, *ApJL*, 567, 115
- Kennicutt, R. C. Jr., 1998, *ARA&A*, 36, 189
- Keres, D., Vogelsberger, M., Sijacki, D., Springel, V. & Hernquist, L., 2012, *MNRAS*, 425, 2027
- King, I., 1962, *AJ*, 67, 471
- Komatsu, E., Smith, K. M., Dunkley, J., et al., 2011, *ApJS*, 192, 18
- Kraft, R. P., Forman, W. R., Jones, C., et al., 2011, *ApJ*, 727, 41
- Kuntz, K. D. & Snowden, S. L., 2000, *ApJ*, 543, 195
- Li, Z. & Wang, Q. D., 2007, *ApJ*, 668, L39
- Li, J.-T., Li, Z., Wang, Q. D., Irwin, J. A. & Rossa, J., 2008, *MNRAS*, 390, 59
- Li, Z., Jones, C., Forman, W. R., 2011, *ApJ*, 730, 84
- Lumb, D. H., Warwick, R. S., Page, M. & De Luca, A., 2002, *A&A*, 389, 93
- Mathews, W. G. & Brighenti, F., 2003, *ARA&A*, 41, 191
- Mandelbaum, R., Seljak, U., Kauffmann, G., Hirata, C., M. & Brinkmann, J., 2006, *MNRAS*, 368, 715
- Meurer, G. R., Heckman, T. M. & Calzetti, D., 1999, *ApJ*, 521, 64
- Navarro, J. F., Frenk, C. S. & White, S. D. M., 1997, *ApJ*, 490, 493
- Nevalainen, J., Markevitch, M. & Lumb, D., 2005, *ApJ*, 629, 172
- Nulsen, P. E. J., McNamara, B. R., Wise, M. W. & David, L. P., 2005, *ApJ*, 628, 629
- Oppenheimer, B. D. & Davé, R., 2006, *MNRAS*, 373, 1265
- Paturel, G., Petit, C., Prugniel, P., et al., 2003, *A&A*, 412, 45
- Predehl, P., Andritschke, R., Böhringer, H., et al., 2010, in *SPIE Conf. Ser.*, 7732
- Randall, S. W., Forman, W. R., Giacintucci, S., et al., 2011, *ApJ*, 726, 86
- Rasmussen, J., Sommer-Larsen, J., Pedersen, K., et al., 2009, *ApJ*, 697, 79
- Revnivtsev, M., Churazov, E., Sazonov, S., Forman, W. & Jones, C., 2008, *A&A*, 490, 37
- Sarazin, C. L., Irwin, J. A. & Bregman, J. N., 2001, *ApJ*, 556, 533
- Sanders, D. B., Mazzarella, J. M., Kim, D.-C., Surace, J. A. & Soifer, B. T., 2003, *AJ*, 126, 1607
- Schaye, J., Dalla Vecchia, C., Booth, C. M., et al., 2010, *MNRAS*, 402, 1536
- Sijacki, D.; Springel, V., Di Matteo, T., & Hernquist, L., 2007, *MNRAS*, 380, 877
- Sijacki, D., Vogelsberger, M., Keres, D., Springel, V. & Hernquist, L., 2012, *MNRAS*, 424, 2999
- Silk, J. & Rees, M. J., 1998, *A&A*, 331, L1
- Springel, V., 2005, *MNRAS*, 364, 1105
- Springel, V., 2010, *MNRAS*, 401, 791
- Springel, V. & Hernquist, L., 2002, *MNRAS*, 333, 649
- Springel, V. & Hernquist, L., 2003, *MNRAS*, 339, 289
- Starck, J.-L., Fadili, J. M., Digel, S., Zhang, B. & Chiang, J., 2009, *A&A*, 504, 641
- Strickland, D. K., Heckman, T. M., Colbert, E. J. M., Hoopes, C. G. & Weaver, K. A., 2004a, *ApJS*, 151, 193
- Strickland, D. K., Heckman, T. M., Colbert, E. J. M., Hoopes, C. G. & Weaver, K. A., 2004b, *ApJ*, 606, 829
- Sun, M., Jones, C., Forman, W., et al., 2007, *ApJ*, 657, 197
- Toft, S., Rasmussen, J., Sommer-Larsen, J., Pedersen, K., 2002, *MNRAS*, 335, 799
- Torrey, P., Vogelsberger, M., Sijacki, D., Springel, V. & Hernquist, L., 2011, arXiv:1110.5635
- van de Voort, F., Schaye, J., Booth, C. M., Haas, M. R. & Dalla Vecchia, C., 2011, *MNRAS*, 414, 2458
- Vikhlinin, A., Kravtsov, A., Forman, W., et al., 2006, *ApJ*, 640, 691
- Vikhlinin, A., Reid, P., Tananbaum, H., et al., 2012, in *SPIE Conf. Ser.*, 8443
- Vogelsberger, M., Sijacki, D., Keres, D., Springel, V. & Hernquist, L., 2012, *MNRAS*, 425, 3024
- Wang, Q. D., 2005, *ASPC*, 331, 329
- White, S. D. M. & Frenk, C. S., 1991, *ApJ*, 379, 52
- White, S. D. M. & Rees, M. J., 1978, *MNRAS*, 183, 341
- Zhang, Z., Gilfanov, M. & Bogdán, Á., 2012, arXiv:1211.0399